LARGE EDDY SIMULATION OF SYNGAS-AIR DIFFUSION FLAMES WITH ARTIFICIAL NEURAL NETWORKS BASED CHEMICAL KINETICS

A Thesis
Presented to
The Academic Faculty

by

Anuradha Sanyal

In Partial Fulfillment
of the Requirements for the Degree
Master of Science in
Aerospace Engineering

School of Aerospace Engineering
Georgia Institute of Technology
December 2011

LARGE EDDY SIMULATION OF SYNGAS-AIR DIFFUSION FLAMES WITH ARTIFICIAL NEURAL NETWORKS BASED CHEMICAL KINETICS

Approved by:

Professor Suresh Menon, Advisor
School of Aerospace Engineering
Georgia Institute of Technology

Professor Jeff I. Jagoda
School of Aerospace Engineering
Georgia Institute of Technology

Professor Stephen M. Ruffin
School of Aerospace Engineering
Georgia Institute of Technology

Date Approved: 26 August 2011

ACKNOWLEDGEMENTS

First and foremost I want to thank my advisor Dr. Suresh Menon. It has been an honor to be his student at Computational Combustion lab. Working under his guidance has been an enormous learning experience for me. I appreciate all his contributions of time, ideas, and funding to make my MS experience productive and stimulating. I would like to thank my reading committee members: Dr. Jeff Jagoda and Dr. Stephen Ruffin for their time, interest and helpful commments. I greatfully acknowledge NASA for the funding that made my MS work possible.

I would like to thank current and past CCL colleagues: Dr. Franklin Genin, Dr. Kaushik Balakrishnan, Dr. Jung Choi, Dr. Srikant Srinivasan, Kalyana Gottiparthi, Andy Smith, Tim Gallagher, Orcun Kozaka, Leandro Gryn-garten, Satoshi Ukai, Joey Schluz, Chaitanya Ghodke and Alpha Bah who helped me understand the models and code used in the lab. I am particularly indebted to Dr. Baris Ali Sen and Matthieu Masquelet who have helped me a lot in understanding the physics, and to Ramya Pasumarti, who has been a close friend.

I would like to thank my parents, Manas Sanyal and Rita Sanyal for their love and support. Last but not the least I would like to thank Dr. Shiladitya Mukherjee, my husband for his continuous encouragement and support.

TABLE OF CONTENTS

LIST OF TABLES

LIST OF FIGURES

NOMENCLATURE

Abbreviations

$AGDR$ Adaptive Gradient Descent Rule

AN Artificial Neuron

ANN Artificial Neural Network

CMC Conditional Moment Closure

DI Direct Integration

$DI-LEMLES$ DI used to compute the laminar source term in the LEM subgrid combustion model within the LES framework

DNS Direct Numerical Simulation

GDR Gradient Descent rule

$LANN$ Laminar (instantaneous) Artificial Neural Network

$LANN-LEMLES$ LANN used to compute the laminar source term in the LEM subgrid combustion model within the LES framework

$LDKM$ Localized Dynamic k-equation Model

LEM Linear Eddy Mixing

$LEMLES$ LEM used as a subgrid combustion model within the LES framework

LES Large Eddy Simulation

MMC Multiple Mapping Conditioning

PDF Probability Distribution Function

PE Processing Element

$TANN$ Turbulent (filtered) Artificial Neural Network

$TANN - LES$ TANN used to compute the filtered source term directly within the LES framework

Subscripts

LEM quantity related to LEM scale

Greek Symbols

α thermal diffusivity or the global momentum coefficient for ANN

χ scalar dissipation rate based on mixture fraction

χ_{st} scalar dissipation rate on stoichiometric plane

Δ_t time step size

δ_{ij} Kronecker delta

$\delta_m[k]$ local error term of Processing Element m at k-th iteration

Δ_{diff} diffusion time step size

Δ_{stir} stirring time step size

$\dot{\omega}_i$ chemical reaction rate of the i-th species

ϵ rate of dissipation of turbulent kinetic energy

η_k pure viscosity of the k-th species

η Kolmogorov length scale or the global learning coefficient in ANN

κ thermal conductivity

λ_k pure conductivity of the k-th species

λ stirring frequency

μ mixture viscosity

ν_t turbulent viscosity

$\Omega^{(1,1)}$ correction factor

$\overline{\Delta}$ large eddy simulation grid cut-off scale

$\phi_{ij}[k]$ gradient of training error w.r.t. weight coefficient joining AN pair i and j

ρ density

ρ_t density at time instant t

τ_{ij} viscous stress tensor

D_k^T thermal diffusion coefficient of the k-th species

D_{jk} binary diffusion coefficient of the species i and j

k_B Boltzman constant

$\dot{\omega_T}$ heat release rate due to combustion

Others

$\widehat{\ }$ test filter

$\widetilde{\ }$ Favre spatial filter

$\bar{\ }$ space average

Roman Symbols

$(D_k)_m$ mixture averaged diffusion coefficient of the k-th species

b_i bias value of Artificial Neuron i

C_ν model coefficient for turbulent viscosity

C_ϵ model coefficient for subgrid dissipation

$c_{p,k}$ specific heat at constant pressure per unit mass of the k-th species

D^{sgs} dissipation of subgrid turbulent kinetic energy

D_i molecular diffusivity of the i-th species

d_i desired output for the Artificial Neural Network training

Da Damkohler number

E total energy

e internal energy

$E[k]$ Artificial Neural Network training error at the k-th iteration

$F_{k,stir}$ turbulent stirring for k-th species in LEM species equation

$F_{T,stir}$ turbulent stirring for temperature in LEM energy equation

h_k species enthalpy per unit mass of k-th species

$J_{i,k}$ diffusion flux of the k-th species in the i-th direction

k^{sgs} subgrid turbulent kinetic energy

l integral length scale

L_{ij} Leonard's stress

m_{ij} reduced molecular mass of the species pair i and j

N_s number of species

net_i	input signal received by i-th Artificial Neuron
p	pressure
P^{sgs}	production of subgrid turbulent kinetic energy
Pr	Prandtl number
q_i	heat flux in the i-th direction
R_u	universal gas constant
Re	Reynold's number
Re_Δ	subgrid Reynold's number
S	strain rate
Sc_t	turbulent Schmidt number
T	temperature
t	time
u'	rms velocity
u_i	velocity in i-th direction
V_i^C	correction velocity in the i-th direction
$V_{i,k}$	diffusion velocity of the k-th species in the i-th direction
W_k	molecular weight of the k-th species
W_{ji}	strength of weight connection between Artificial Neuron pair i and j
x_i	Cartesian coordinate in i-th direction
X_k	mole fraction of the k-th species

$Y_k^{t+\Delta t}$ mass fraction of k-th species at time instant $t + \Delta t$

Y_k^t mass fraction of k-th species at time instant t

Y_i mass fraction of the i-th species

y_n output of the n-th Artificial Neuron

Z mixture fraction

g() activation function used by an Artificial Neuron

Superscripts

R resolved subgrid fluctuation

S unresolved subgrid fluctuation

sgs subgrid scale

", ' fluctuating quantity

SUMMARY

In the present study syngas-air diffusion flames are simulated using LES with artificial neural network (ANN) based chemical kinetics modelling and the results are compared with previous direct numerical simulation (DNS) study [14], with the objective of obtaining speed-up in chemistry computation while still having the accuracy of a stiff ODE solver. The DNS test case exhibits significant extinction-reignition and forms a challenging problem for ANN. The ANN methodology is used in two ways: 1) to compute the instantaneous source term in the linear eddy mixing (LEM) subgrid combustion model used within LES framework, i.e., laminar-ANN used within LEM-LES framework (LANN-LEMLES, hereafter), 2) to compute the filtered source terms directly within the LES framework, i.e., turbulent-ANN used within LES (TANN-LES, hereafter), which further increases the computational speed. A thermo-chemical database is generated from a standalone one-dimensional LEM simulation and used to train the LANN for species source terms on grid-size of Kolmogorov scale [34]. To train the TANN coefficients the thermo-chemical database from the standalone LEM simulation is filtered over the LES grid-size and then used for training [32]. To evaluate the performance of the TANN methodology, the low Re test case is simulated with direct integration used for chemical kinetics modelling in LEM subgrid combustion model within the LES framework (DI-LEMLES, hereafter), LANN-LEMLES and TANN-LES. The TANN is generated for a low range of Re_t in order to simulate the specific test case. The conditional statistics and pdfs of key scalars and the temporal evolution of the temperature and scalar dissipation rates are compared with the data extracted form DNS. Results show that the TANN-LES methodology can capture the extinction-reignition physics with reasonable accuracy compared to the DNS. Another

TANN is generated for a high range of Re_t expected to simulate test cases with different Re and a range of grid resolutions. The flame structure and the scalar dissipation rate statistics are analysed to investigate success of the same TANN in simulating a range of test cases. Results show that the TANN-LES using TANN generated for a large range of Re_t is capable of capturing the extinction-reignition physics with a very little loss of accuracy compared to the TANN-LES using TANN generated for the specific test case. The speed-up obtained by TANN-LES is significant compared to DI-LEMLES and LANN-LEMLES.

CHAPTER I

INTRODUCTION

In non-premixed flames the heat release rate is controlled by the molecular mixing rate of fuel and oxidizer, which is a process occurring at small scales and hence, the combustion process essentially takes place at small scales. However, the large scale convection process due to turbulence enhances the rate of fuel-oxidizer mixing by straining and affects the combustion process. The rate of fuel-oxidizer mixing is characterized by scalar dissipation rate[29] which is a function of molecular diffusivity D and gradient of mixture fraction Z [1]. Initially as χ increases the rate of molecular mixing increases and the rate of burning also increases. However, if χ exceeds a critical value (extinction scalar dissipation rate, χ_q) over prolonged periods of time, then the diffusive heat loss becomes greater than the rate of heat release due to chemical reactions leading to temperature drop and reactants leaking through the reaction zone resulting in local extinction. The mixing process continues during this period and local packets of partially premixed and non-premixed mixtures are formed. This mixture can either reignite on its own once χ reduces or by coming close to burning regions in the surroundings. Understanding the extinction-reignition phenomenon is important because modern combustion systems require efficient mixing for enhanced burning which is obtained by increasing χ. However, large values of χ leads to extinction-reignition process which destabilizes the flame and also increases emissions due to incomplete combustion [29].

1.1 Flame-Turbulence Interaction

Previous direct numerical simulation (DNS) studies [36, 37, 14, 27] have investigated the extinction-reignition process in turbulent non-premixed flames. Sripakagorn et al. [36, 37] in their studies of non-premixed combustion in decaying isotropic turbulence using one-step global reaction, observed that the average scalar dissipation rate at stoichiometric mixture fraction (χ_{st}) remained lower than the extinction scalar dissipation rate even though the fluctuations of the instantaneous χ_{st} showed large values over χ_q causing local extinction events. They observed that reignition occurs due to three reasons: 1) once the χ_{st} drops the flamelet reignites on its own (independent flamelet scenario), 2) edge flame propagation, 3) a hot neighbourhood engulfs the unburnt packet. Besides, the probability of reignition is highest due to independent flamelet scenario. Pantano et al.[27] in their studies of methane-air diffusion flames showed that higher order reaction mechanisms are needed for detailed investigation of extinction-reignition phenomenon. Hawkes et al.[14] studied temporally evolving syngas-air diffusion flames with significant extinction-reignition. They used an 11 species, 21 steps skeletal reaction mechanism to study the evolution of flame structure and the characteristic of mixture fraction Z and showed that the predictions with the skeletal mechanism is in good agreement with the detailed mechanism.

Modelling the spatially filtered chemical source terms and the turbulence-chemistry interaction forms a challenging problem in LES since combustion process is a small scale process [29, 28]. DesJaridin et al. [10] showed that modelling the reaction term by directly using the filtered resolved scales in the chemical kinetics model gives poor agreement when compared with DNS results. This is observed when chemical reaction rates are comparable with the rate of mixing, i.e., the turbulence-chemistry interaction is strong and hence the subgrid fluctuations of the scalar field can no longer be neglected.

Various closure models have been studied in the past. Joint PDF methods provide

exact closure to the source terms, but increase in the number of species increases the dimensionality of the joint PDF and makes it expensive. Besides, the molecular diffusion terms are unclosed and the quality of the predictions depend on the applied mixing model and the values of the constants used [39]. Multiple mapping conditioning (MMC) is a cheaper option which reduces the dimensions of the reference space depending on the problem and captures extinction-reignition with reasonable accuracy. However, choosing the reference space is a challenging task. Cleary et al. [9] in their studies of turbulent non-premixed flames showing extinction-reignition used a single mixture-fraction-like variable and up to three dissipation like variables. Results showed poor accuracy of the model in case of moderate extinction-reignition, even though it predicted significant extinction-reignition and global extinction with reasonable accuracy. First order flamelet model and conditional moment closure (CMC) model singly conditioned on mixture-fraction with first moment closure reduces the dimensionality to one but breaks down when extinction-reignition phenomenon are present [29],[23]. Because in singly conditioned CMC model with first order closure approximation only the average χ_{st} appears and the fluctuations of χ_{st} are neglected. Hence close to extinction-reignition where the fluctuations of χ_{st} are large the model breaks down. CMC closure based on a precomputed parameterized reference field that maps reactive species mass fractions as functions of mixture fraction and sensible enthalpy have successfully captured the extinction-reignition phenomenon [24]. However, this requires the reference field to be continuously adjusted during computation, to ensure consistency with the CMC solution and doubly conditioned chemical source terms that are functions of time, space, mixture fraction, and sensible enthalpy can thus be obtained.

The flamelet model assumes the PDF of mixture fraction and scalar dissipation rate at stoichiometric mixture fraction (χ_{st}) as marginal beta and log-normal distributions, respectively, which do not hold good near extinction-reignition scenarios where there

are high levels of chemical non-equilibrium [13]. Pitsch et al. [30] studied the influence of stochastic fluctuations of the scalar dissipation rate on the solution of the flamelet equations and suggested a new transport term in the flamelet equations modelled by a stochastic mixing approach and an additional stochastic differential equation for the scalar dissipation rate. Second order CMC models have shown improvement in capturing extinction-reignition phenomenon in hydrocarbon jet diffusion flames using detailed kinetics[20]. However, additional equations for the conditional variances and covariances of each pairing of reactive species are required, which makes CMC expensive for detailed reaction mechanisms. Besides, the second order correlations need to be determined from DNS data. First order CMC model doubly conditioned on mixture fraction and scalar dissipation rate is another alternative; however, it predicts the onset of reignition too early [4].

Linear eddy mixing (LEM) model used as a subgrid combustion model within LES framework (LEMLES) closes the reaction-diffusion equation in an exact sense and captures extinction-reignition with accuracy [32]. However, using LEM model with the stiff ODE solver to find source terms is computationally expensive.

To reduce the cost of chemical kinetics evaluation in LEMLES, Sen et al. [32] used an artificial neural networks (ANN) based chemical kinetics modelling, which eliminates the stiff ODE solver to calculate the subgrid laminar reaction rates (LANN).

1.2 Artificial Neural Networks (ANN)

Artificial neural networks are modelled after the biological neurons [25]. The ANN is made of a number of simple highly interconnected processing elements (PEs) which process information by its dynamic state response to external inputs. It is an interpolation scheme. Contrary to the conventional approach of solving equations, ANN learns by example and provides predictions into new states. An ANN architecture is as shown in Fig. 1. The large circles are the Processing Elements (PEs) and the lines

joining them are the weight connectors. The first layer of PEs from left is the input layer, the middle two layers of PEs are the hidden layers, and the fourth layer is the output layer. The set of input/output pairs of PEs are representative of the physical process. The purpose of the hidden layers is to make the ANN capable of modelling complex data. Choosing the correct number of processing elements in a hidden layer is another challenging task. If an inadequate number of processing elements are used in a hidden layer, the net will not be able to model complex data. On the other hand, if too many neurons are used, training time will become excessively long and the model may memorize the data. This result in ANN net fitting the data for which is trained extremely well but generalizing poorly to new unseen data. In the given example, the N number of inputs, which include mass fraction of all the species and temperature, are used to compute the species reaction rate of H_2, by interpolation.

Fig.2 show two AN pairs. Each connection between a particular AN (Artificial

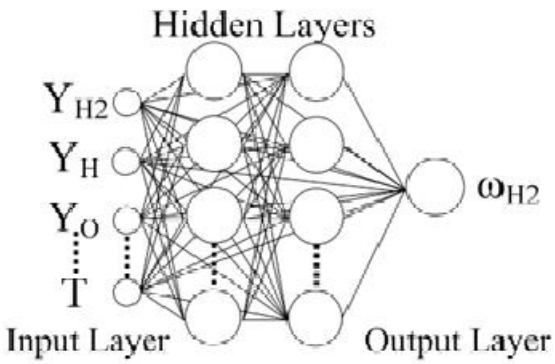

Figure 1: Representation of an Artificial Neural Network Architecture

Neuron) pair (i and j) has a weight coefficient W_{ji}, which defines the strength of the connection between the AN pair. The combined effect of all ANs connected to AN_i, acting as an input vector for AN_i is:

$$net_i = \sum_{j=0}^{J} W_{ij}\,[k]\,y_j - b_i \tag{1}$$

where y_j is the signal fired from AN_j to AN_i and W_{ij} is the respective weight coefficient and b_i represents the internal threshold for the AN_i. The net output of AN_i is:

$$y_i = g\left(net_i\right) \tag{2}$$

where g is an activation function. For a given ANN architecture and input/output

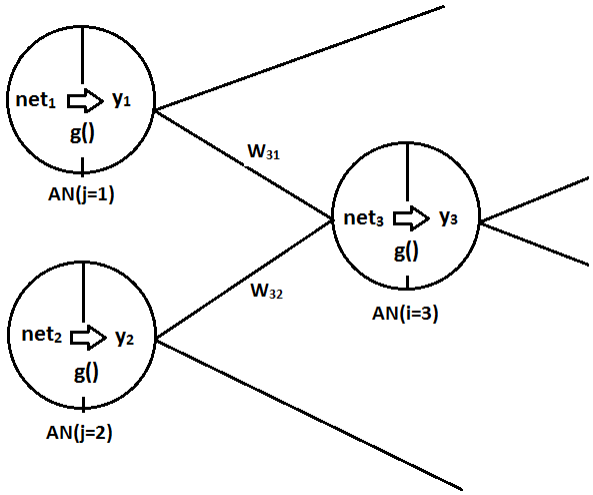

Figure 2: Description of Artificial Neuron pairs

pairs, the weight coefficients are determined through a training process. The objective is to train long enough such that the ANN predicts well for both train and test data, while not so long that the ANN memorizes the train data, giving very good predictions for train data and poor predictions for test data. Hence, it is important to stop the training at the correct time because long training times may again lead to memorization of data. In the present study if the training error does not reduce for 100 consecutive sweeps of the training table, the training is stopped and the weight coefficients calculated before last 100 sweeps are used in the ANN.

Past studies have successfully used ANN for function approximation, classification, time series prediction, data association, optimization in a variety of applications such as, electro magnetics [7], forecasting [40], land cover classification and mapping [8] and chemical kinetics modelling with significant memory savings and speed-up. Christo

et al. [6] used artificial neural networks (ANN) model based chemical kinetics for a systematically reduced H_2-CO_2 system, consisting of three steps and four controlling scalars. The ANN was implemented with transported-PDF (Monte Carlo) approach. Blasco et al. [2] in addition to simulating the species evolution, used ANN for providing the density and temperature. Ihme et al. [16] proposed a generalized method for the generation of optimal artificial neural networks. They tested it with the methane-hydrogen/air flame in a bluff-body swirl-stabilized burner configuration using LES to investigate the effect of long-time error accumulation in the statistical data during the simulation[17]. However all these studies generated the training table for ANN by either three-dimensional simulations of cases similar to the actual test case or randomly generating compositions within allowable compositional bounds. These compositional bounds have to be selected carefully for an efficient ANN and are specific to a problem. Further, the random selection of training samples lead to bias of the training set towards the steady state situation and a better selection criteria based on the degree of chemical activity of a state had to be used.

Sen et al. [34] generated the training table for ANN by using off-line (standalone 1D) LEM computations. This table did not require any compositional bounds and did not show any bias towards steady state. The ANN was trained using this table. The ANN generated was used in the LEMLES simulation to compute the laminar reaction rates. Hence, ANN was generated without a-priori knowledge of the actual thermochemical data space of test case. To further reduce the cost of computation, Sen [35] used the off-line LEM computations, but instead of tabulating the laminar reaction rates, the filtered reaction rates representative of the LES were tabulated along with the filtered thermochemical data [35]. Hence, the trained ANN (TANN) directly estimated the filtered reaction rates within the LES framework and eliminated the need of LEM with significant cost reduction. In the current effort, the TANN approach is further analysed, to investigate the development of a general TANN to simulate a

range of cases with varying Reynolds number and grid resolutions. Further, the key parameters affecting the development of the general TANN is analysed.

1.3 Objectives

Syngas or synthetic gas mixtures can be produced from a wide variety of sources including coal, biomass, organic waste, and refinery residuals. It consists of mainly CO and H_2 in various proportions. When derived from biomass and other industrial waste it forms a cheap and renewable source of energy. Because of the large coal resources available worldwide, there is strong interest in coal-based integrated gasification combined cycle power generation. Hence, understanding the behaviour of syngas is very crucial for its industrial usage. This thesis studies the extinction-reignition phenomenon in temporally evolving syngas-air flames using ANN for chemical kinetics modelling. Test cases are chosen from a previous direct numerical (DNS) study of temporally evolving syngas-air diffusion flames with 21 steps, 11 species reduced chemical kinetics[14]. These cases exhibit complex extinction-reignition phenomenon for a range of flow Reynolds number and varying levels of turbulence. The degree of extinction also increases with increase in Re which leads to lower mean temperature and longer re-ignition times. Hence, these cases form a challenging problem for the development of a general TANN. The main objective is to obtain considerable speed-up while having the same accuracy as DI. The objectives in details are as follows:

- Study extinction-reignition in non-premixed flames using ANN for laminar (instantaneous) reaction rates (LANN) with LEMLES framework.

  To evaluate the accuracy and speed-up of the ANN methodology, it is used to simulate a temporally evolving jet flame for a low Reynolds number case. A

DNS study is selected as the test case from literature [14]. The thermochemical database for training ANN is generated using a one-dimensional standalone LEM computation, instead of using actual LES simulation data. The standalone LEM covers a wide range of flame-turbulence interaction. It is expected that it will cover a large thermo-chemical data space and the thermochemical data space of the LES simulation will form just a subset of the LEM thermochemical data space. Hence, the ANN for computing the instantaneous reaction rates can be generated without a-priori knowledge of the LES thermochemical data space. The instantaneous reaction rate is obtained as a function of temperature and species concentration.

$$\frac{\dot{\omega}_i}{\rho} = f\left(Y_1, ..., Y_{N_s}, T\right) \text{ where, i=1,....,} N_s \tag{3}$$

For a given pressure and LEM time step size (Δt)

The source terms in the subgrid combustion model within the LEMLES simulation is computed using ANN. The conditional PDFs of the species extracted from the LANN-LEMLES and compared with the DI-LEMLES and DNS study to evaluate the accuracy of the LANN generated. The evolution of the scalar-dissipation PDFs during extinction and reignition are also investigated.

- Study extinction-reignition in non-premixed flames using ANN for filtered reaction rates (TANN).

  To further increase, the speed-up of the LES simulation, ANN is trained to calculate the filtered reaction rates directly within the LES framework. Using the standalone LEM, the filtered reaction rates are tabulated by applying a spatial filter on the 1D LEM domain data. The filtered reaction rate is trained in the ANN as a function of filtered mass fractions, temperature, subgrid Reynolds number, and filtered level species gradient. A fixed filter size representative of the LES grid size is used for spatial filtering. The filtered source term is trained

as a function of the subgrid Re and filtered species gradient to take into account the effect of turbulence.

$$\frac{\overline{\dot{\omega}}_i}{\overline{\rho}} = f\left(\widetilde{Y}_1, ..., \widetilde{Y}_{N_s}, \widetilde{T}, Re_\Delta, \frac{\partial \widetilde{Y}_i}{\partial x_j}\right) \text{ where, i=1,....,} N_s \tag{4}$$

For a given pressure, filter size and LES time step size (Δt)

The TANN is used to calculate the filtered reaction rates in the LES simulation of the temporally evolving syngas-air jet flames and the results are compared with the DNS study to evaluate the accuracy of TANN.

- Study extinction-reignition in non-premixed flames using a single TANN for a range of cases.

  The TANN approach is explored further and a generalized TANN net is developed by training it over data collected from standalone LEM simulation run over a large range of Re_t. This TANN net is used to simulate a range of cases with varying Reynolds number and grid resolutions. The success of a generalized TANN net for a range of cases will lead to significant time savings. Otherwise, every new a case will require generation of a new TANN which will consume time and resources.

- Study extinction-reignition using TANN trained as a function of species scalar dissipation rate.

  The filtered reaction rate is obtained from the ANN as a function of filtered mass fractions, temperature, subgrid Reynolds number and filtered level species dissipation rate. The use of filtered level species dissipation rate instead of species gradient is more relevant to modelling filtered species reaction rate, because lighter species have higher molecular diffusivity D, and for for the same species gradient dissipate much faster than the heavier species and affect the

filtered source term largely.

$$\frac{\overline{\dot{\omega}}_i}{\overline{\rho}} = f\left(\widetilde{Y}_1, ..., \widetilde{Y}_{N_s}, \widetilde{T}, Re_\Delta, 2D_i \frac{\partial \widetilde{Y}_i}{\partial x_j}.\frac{\partial \widetilde{Y}_i}{\partial x_j}\right) \text{ where, } i = 1, ..., N_s \qquad (5)$$

The results obtained are compared with the DNS study and TANN-LES trained as a function of species gradient instead of species scalar dissipation rate.

CHAPTER II

COMPUTATIONAL MODELLING

In the present chapter, first the general Navier-Stokes equations are described. Second the stand-alone LEM modelling is described. The stand-alone LEM simulation is used to generate the thermochemical data for training the ANN without a-priori knowledge of the actual 3D simulation. Third the tabulation method for TANN is described. Fourth, ANN architecture and its training is described. Finally the LES modelling and subgrid combustion modelling is explained.

2.1 Gas Phase Governing Equations

The gas phase governing equations of continuity, momentum, energy and species in the conserved form, in the absence of external forces, MHD effects, etc, are given as:

$$\begin{aligned}
\frac{\partial \rho}{\partial t} + \frac{\partial \rho u_i}{\partial x_i} &= 0 \\
\frac{\partial \rho u_i}{\partial t} + \frac{\partial}{\partial x_j}[\rho u_i u_j + p\delta_{ij} - \tau_{ij}] &= 0 \\
\frac{\partial \rho E}{\partial t} + \frac{\partial}{\partial x_i}[(\rho E + p)u_i - u_j \tau_{ji} + q_i] &= 0 \\
\frac{\partial \rho Y_k}{\partial t} + \frac{\partial}{\partial x_i}[\rho Y_k u_i + J_{i,k}] &= \dot{\omega}_k
\end{aligned} \tag{6}$$

where, $k = 1, ..., N_s$

In the above equations ρ is the density, u_i is the i-th velocity component, E is the total energy, Y_k is the k-th species mass fraction and N_s represents the total number of species in the flow. τ_{ij} is the viscous stress tensor and is computed as:

$$\tau_{ij} = \mu\left(\frac{\partial u_i}{\partial x_j} + \frac{\partial u_j}{\partial x_i}\right) - \frac{2}{3}\delta_{ij}\mu\frac{\partial u_k}{\partial x_k} \tag{7}$$

where δ_{ij} is the Kronecker function ($\delta_{ij} = 1$ if $i = j$; $\delta_{ij} = 0$ if otherwiese),and μ is the dynamic viscosity. The total energy E is the sum of internal energy (e) and kinetic

energy, is given as:

$$E = e + \frac{1}{2} u_k u_k \tag{8}$$

In this formulation the internal energy per unit mass is:

$$e = \sum_{k=1}^{N_s} Y_k h_k - \frac{p}{\rho} \tag{9}$$

The k-th species total enthalpy is calculated as the sum of the chemical and sensible enthalpies as:

$$h_k(T) = \Delta h^0_{h,k} + \int_{T_0}^{T} c_{P,K}(T')dT' \tag{10}$$

In the above equation $\Delta h^0_{h,k}$ is the enthalpy of formation at the reference temperature and pressure T_0, P_0. The second represents sensible enthalpy, which is a function of temperature and $c_{P,k}$ is the heat capacity at constant pressure for the k-th species.

The pressure in equation (6)is derived from the perfect gas equation of state:

$$p = \rho R_u T \sum_{k=1}^{N_s} \frac{Y_k}{W_k} \tag{11}$$

where, R_u, N_s, W_k are the universal gas constant, number of species and molecular weight of k-th species, respectively.

The mass reaction rate per unit mass ($\dot{\omega}_k$) for the k-th species is calculated by solving the ODE representing a given reaction mechanism. For the given initial concentration of the species and a time step size, the ODE solver is used to find the new scalar field at the end of the time step. The reaction rate is calculated as:

$$\dot{\omega}_k = \frac{(Y_k^{t+\Delta t} - Y_k^t)\rho^t}{\Delta t} \tag{12}$$

The heat flux (q_i) and the k-th species diffusion flux ($J_{i,k}$) introduced in Eq. (6) are defined as:

$$q_i = \sum_{k=1}^{N_s} J_{i,k} h_k - \kappa \bigtriangledown T - \sum_{k=1}^{N_s} \frac{R_u T}{W_k X_k} D^T d_{ik} \tag{13}$$

$$J_{i,k} = \rho Y_k V_{i,k} \tag{14}$$

The last term in Eq.(13) is neglected in the present simulation where D_K^T is the thermal diffusion coefficient. $V_{i,k}$ is the k-th species diffusion velocity. The species diffusion velocity takes into account mass diffusion caused by concentration gradients (ordinary diffusion), temperature gradients (Soret effect) and pressure gradients. In the present study the effect of pressure gradients and temperature gradients is neglected. Mixture-averaged formulation is used to find the diffusion velocity instead of more accurate multi-component formulation, because the latter approximation requires inverting an $N_s \times N_s$ matrix to find the multi-component diffusion coefficients. The diffusion velocity for a mixture averaged formulation is given as:

$$V_{i,k} = -\frac{1}{X_k}(D_k)_m \frac{\partial X_k}{\partial x_i} \tag{15}$$

where the mixture diffusion coefficient for the k-th species is:

$$(D_k)_m = \frac{\sum_{j \neq k}^{N_s} X_j W_j}{W_m \sum_{j \neq k}^{N_s} X_j / D_{jk}} \tag{16}$$

where D_{jk}'s are the binary diffusion coefficients. It assumes a two component binary mixture, where species j is diffusing into species k. Based on kinetic theory of gases, the binary diffusion coefficients are calculated as:

$$D_{jk} = \frac{3}{16} \frac{\sqrt{2\pi k_B^3 T^3 / m_{jk}}}{p\pi \sigma_{jk}^2 \Omega^{(1,1)}} \tag{17}$$

where k_B is the Boltzman constant, σ_{jk} is the mean diameter ($= (\sigma_{jk} + \sigma_{jk})/2$), and $\Omega^{(1,1)}$ is the correction factor used to modify the ideal gas law to account for the molecular interactions. The reduced mass m_{jk} is the given by:

$$m_{jk} = \frac{m_j m_k}{m_j + m_k} \tag{18}$$

The mixture averaged formulation needs to satisfy the net species diffusion flux to zero ($\sum_{k=1}^{N_s} V_{i,k} Y_k = 0$) for conservation of mass. This is done by adding a correction velocity to the convective terms in the species conservation equation to account for

the excess diffusion. The correction velocity is calculated as:

$$V_i^C = -\sum_{k=1}^{N_s} Y_k \left(\frac{1}{X_k} (D_k)_m \frac{\partial X_k}{\partial x_i} \right) \tag{19}$$

With the correction the k-th species diffusion flux is calculated as:

$$J_{i,k} = \rho Y_k \left(V_{i,k} + V_i^C \right) \tag{20}$$

The mixture averaged viscosity given by Vilke's formula:

$$\mu = \sum_{k=1}^{N_s} \frac{X_k \eta_k}{\sum_{k=1}^{N_s} X_j \Phi_{kj}} \tag{21}$$

where

$$\Phi_{kj} = \frac{1}{\sqrt{8}} \left(1 + \frac{W_k}{W_j} \right)^{-\frac{1}{2}} \left(1 + \left(\frac{\eta_k}{\eta_j} \right)^{\frac{1}{2}} \left(\frac{W_j}{W_k} \right)^{\frac{1}{4}} \right)^2 \tag{22}$$

where η_i is the i-th species viscosity. The thermal conductivity is calculated in a similar manner using the following formula:

$$\kappa = \frac{1}{2} \left(\sum_{k=1}^{N_s} X_k \lambda_k + \frac{1}{\sum_{k=1}^{N_s} X_k / \lambda_k} \right) \tag{23}$$

where λ_k is the pure species conductivity.

2.2 Stand-alone LEM

Off-line stand-alone LEM computations are performed to evaluate the scalar field evolution due to the turbulence-chemistry interaction. The following reaction-diffusion equations are solved along a 1D grid initialized with a laminar diffusion flame:

$$\begin{aligned} \rho \frac{\partial Y_k}{\partial t} &= F_{k,stir} - \frac{\partial}{\partial s} \left(\rho Y_k V_{k,s} + \rho Y_k V_s^C \right) + \quad \dot{\omega}_k \\ \rho C_p \frac{\partial T}{\partial t} &= F_{T,stir} - \rho \frac{\partial T}{\partial s} \left(\sum_{k=1}^{N_s} C_{p,k} Y_k (V_{k,s} + V_s^C) \right) + \frac{\partial}{\partial s} \left(\kappa \frac{\partial T}{\partial s} \right) + \quad \dot{\omega}_T \end{aligned} \tag{24}$$

In Eq.24 the $\dot{\omega}_k$ represents the reaction rate and $\dot{\omega}_T = -\sum_{k=1}^{N_s} h_k \dot{\omega}_k W_k$ represents the heat release due to combustion, where W_k denotes the molecular weight of the k-th species. The reaction rates are obtained by direct integration of the chemical kinetics

model. $V_{k,s} = -D_{k,m}(W_k/WY_K)(\partial X_k/\partial s)$ is the diffusion velocity of the k-th species, diffusivity of the k-th species in the mixture is $D_{k,m} = \left(\sum_{j\neq k}^{N_s} X_j W_k\right)/W \sum_{j\neq k}^{N_s} X_j/D_{j,k}$, where W represents the mixture molecular weight and $D_{j,k}$ represents the binary diffusion coefficient and V_s^C is the velocity correction to ensure mass conservation[31]. Turbulent advection is symbolically represented by $F_{k,stir}$ and $F_{T,stir}$ and modelled as numerical re-arrangement events (triplet-maps)[18]. The assumption behind the stirring model is that, the turbulent advection stochastically re-distributes the concentration gradients, without changing the scalar values and increases the scalar gradients and the molecular diffusion competes with it by smoothing them out. The reaction-diffusion equation proceeds at a time step size determined as $\Delta t_{diff} = 0.25(\Delta s)^2/max(D_k, \alpha)$. Turbulent stirrings proceed at its own time-scale given by $\Delta t_{stir} = 1/(\lambda L)$, where $\Delta s, \alpha, \text{Ł}, \lambda$ denote the LEM grid resolution, thermal diffusivity, LEM domain length and stirring frequency, respectively.

2.3 Tabulation method for TANN and training

The LEM simulation is initialized with a laminar profile obtained for a given themochemical composition and the turbulence-chemistry interaction is simulated for a given range of Re_t. For LANN, the training database was constructed by tabulating the instantaneous composition and temperature from the LEM domain at regular intervals of time along with the laminar reaction rates obtained by directly integrating the chemical kinetics [34],[33]. The tabulation strategy for TANN differs slightly. The results here are filtered by a spatial filter size representative of the LES grid resolution. Fig. 3 shows the variation of the mixture fraction along the 1D LEM domain at a given instant of time. Larger gradients are observed at the LEM level, whereas a smoother profile is observed at the LES level because the spatial filtering process smoothens the effect of large gradients at small scales on an average sense.

In the earlier study [34], the laminar reaction rate was parametrized with respect to the instantaneous species mass fractions and temperature:

$$\frac{\dot{\omega}_i}{\rho} = f(Y_k, T) \tag{25}$$

However, the filtered reaction rates are functions of the LES filter size and turbulence, in addition to the filtered mass fractions and temperature. Hence, filtered reaction rates are parametrized as:

$$\frac{\overline{\dot{\omega}_i}}{\overline{\rho}} = f\left(\widetilde{Y}_k, \widetilde{T}, Re_\Delta, \frac{\partial \widetilde{Y}_i}{\partial x}\right) \tag{26}$$

where, $\widetilde{Y}_k, T$ and $\frac{\partial \widetilde{Y}_i}{\partial x}$ represent the filtered species mass fractions, filtered temperature and filtered species gradient. RE_Δ denotes the sub grid Reynolds number in the LES framework and is calculated as $Re_\Delta = u'\Delta/\nu$, where $u' = \sqrt{(2/3)k^{sgs}}$ and Δ is the LES grid filter. In the stand-alone LEM simulation, based on the Re_t and l_0 (integral lentgth scale) the other parameters like grid spacing, stirring length and stirring frequency are selected [18]. However, Re_t is a global variable for the stand-alone LEM and it differs from local variable Re_Δ in the LES. Stand-alone LEM provides the scalar field evolution and does not provide any information about the local turbulence levels. To calculate Re_Δ the values of kinetic energy k and u' are initially set equal to zero in the LEM domain. Then as the simulation proceeds and turbulent stirrings take place, u' is updated by value $\frac{\nu Re_t}{\eta}$ during a stirring event at the grid locations where it occurs. The turbulence is assumed to be homogeneous and u' in all the three directions is assumed equal, which is consistent with LEM assumption based on universal nature of small scales. The effect of dissipation is

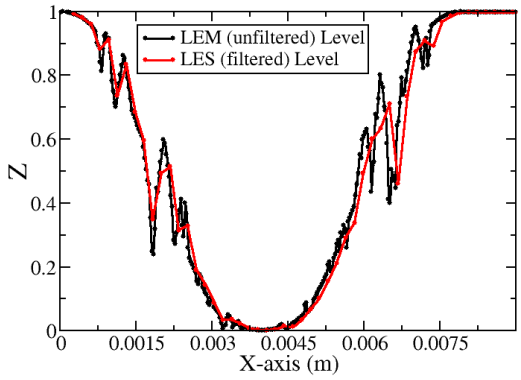

Figure 3: Variation of mixture fraction (Z) along the 1D standalone LEM domain at the DNS level and the LES level

taken into account and the value of u' is updated as follows:

$$\begin{aligned} k &= \frac{3}{2}u'^2 \\ \epsilon &= \frac{k^{1.5}}{\Delta s} \\ k &= Max\left(\left(k - \left(\epsilon * \Delta t_{diff}\right)\right), 0\right) \\ u' &= \sqrt{(2/3)k} \end{aligned} \tag{27}$$

The Re_Δ is calculated as a function of the u' (obtained from Eq. 27), ν averaged over the filtered grid size and the filtered grid size.

The TANN table generated is used to train a given ANN architecture. Finally, the TANN chemical kinetics model is used with in the LES frame work to calculate the filtered reaction rates (TANN-LES).

2.4 Artificial Neural Networks

An acyclic ANN architecture is used in the present study with a predefined number of hidden layers and processing elements [35, 34]. The ANN code based on back-propagation learning with gradient descent rule is used in the present study. The

training algorithm consists of two parts: a) forward propagation of the input, b) backward propagation of the error. The output of a processing element i at iteration k is given as:

$$y_i[k] = g\left(net_i[k]\right) \tag{28}$$

where

$$g\left(z\right) = \frac{e^z - e^{-z}}{e^z + e^{-z}} \tag{29}$$

where $g\left(\right)$ is the hyperbolic tangent activation function. net_i in Eq. 28 represents the effect of all PEs connected to the PE i. net_i is calculated as:

$$net_i[k] = \sum_{m=0}^{M} W_{im}[k] y_m[k] - b_i[k] \tag{30}$$

where, $W_{im}[k]$ is the weight coefficient between PEs i and m, $y_m[k]$ is the output of the PE m, $b_i[k]$ is the internal threshold for the PE i and M is the number of PEs connected to the PE i. After calculating the output for all PEs, the global error $E[K]$ defined as the difference between the desired (d_i) and the calculated $(y_i[k])$ value at the output layer,for the current weight distribution, is calculated:

$$E[k] = \frac{1}{2} \sum_{i=1}^{I} \left[d_i - y_i\left[k\right]\right]^2 \tag{31}$$

where I denotes the PE in the output layer. This error is back propagated to all the PEs and the new weight coefficients are calculated using GDR. Weights of the connections are adjusted according to the gradient of the local error across each connection:

$$W_{ij}[k+1] = W_{ij}[k] - \eta \frac{dE[k]}{dW_{ij}[k]} \tag{32}$$

where η is the global learning coefficient which is constant and same for all PEs and iterations. The idea behind the gradient descent rule is to find a particular weight distribution which provides the minimum global error. Eq. 32 calculates the gradient of the error with respect to the individual weights. The gradient of the error with

respect to the weight coefficient for a connection between the output and a hidden layer is:

$$\frac{dE[k]}{dW_{ij}[k]} = -\left[d_i - y_i[k]\right] g'\left(net_i[k]\right) y_i[k] \tag{33}$$

for rest of the connections it is calculated as:

$$\frac{dE[k]}{dW_{ij}[k]} = -\left[\sum_{m=1}^{M} \delta_m[k] W_{mi}[k]\right] g'\left(net_i[k]\right) y_j[k] \tag{34}$$

here $\delta_m[k]$ is the local error term of the PE m. Its value depending on if the PE m is at the output or a hidden layers is given as:

$$\delta_m[k] = \begin{cases} \left[d_m - y_m[k]\right] g'\left(net_m[k]\right) & \text{if output layer} \\ g'\left(net_m[k]\right) . \sum_{z=0}^{Z} W_{zm}[k]\delta_z[k] & \text{if hidden layers} \end{cases} \tag{35}$$

The error surface may have local minima and a momentum coefficient (α) is used to find the global minimum. The eq. 32 is modified as:

$$\Delta W_{ij}[k] = -\eta \triangle E[k] + \alpha \Delta W_{ij}[k-1] \tag{36}$$

The momentum coefficient (α) like the learning rate coefficient (η) is also the same for all the PEs and constant for all iterations.

The determination of the proper values of the model coefficients (η, α) is a major challenge of the standard GDR. A large α causes the algorithm to diverge and a same η cannot be used in the valleys or shallow regions of the error surface topology. An AGDR approach for self determining the model coefficients with respect to the error surface topology is used in the present work [35]. This method is based on the fact that all PEs have their own model parameters (η_{ij} and α_{ij}) and they are updated at every ANN iterations. The model coefficients are updated as:

$$\begin{aligned} \eta_{ij}[k+1] &= \eta_{ij}[k] + \Delta\eta_{ij}[k] \\ \alpha_{ij}[k+1] &= \alpha_{ij}[k] + \Delta\alpha_{ij}[k] \end{aligned} \tag{37}$$

where $\Delta\eta_{ij}[k]$ and $\Delta\alpha_{ij}[k]$ are calculated as:

$$\Delta\eta_{ij}[k] = \begin{cases} \kappa_1\lambda\eta_{ij} & \text{if } \phi_{ij}[k]\bar{\phi}_{ij}[k-1] > 0 \\ -\kappa_1\lambda\eta_{ij} & \text{if } \phi_{ij}[k]\bar{\phi}_{ij}[k-1] < 0 \\ 0 & \text{if } \phi_{ij}[k]\bar{\phi}_{ij}[k-1] = 0 \end{cases}$$

$$\Delta\alpha_{ij}[k] = \begin{cases} \kappa_1\lambda\alpha_{ij} & \text{if}\phi_{ij}[k]\bar{\phi}_{ij}[k-1] > 0 \\ -\kappa_1\lambda\alpha_{ij} & \text{if}\phi_{ij}[k]\bar{\phi}_{ij}[k-1] < 0 \\ 0 & \text{if}\phi_{ij}[k]\bar{\phi}_{ij}[k-1] = 0 \end{cases} \tag{38}$$

where $\lambda = (1 - exp\,(-\kappa_2\phi_{ij}[k]))$, $\phi_{ij}[k] = \frac{\partial E}{\partial W_{ij}}$ and $\bar{\phi}_{ij}[k] = (1-\theta)\,\phi_{ij}[k-1] + \theta\phi_{ij}[k]$. Here κ_1 and κ_2 are the second order model coefficients selected to be 0.1 and 0.01, respectively.

2.5 LES Modelling

LES approach is employed to solve the fully compressible, reacting, multi-species, Favre averaged form of the conservation equations. The LES equations are obtained by spatially filtering the Navier-Stokes equations, in order to separate the large geometry dependent scale structures from the small-scale structures which are considered universal. In LES the large scales are fully resolved where as the small scales (subgrid-scales) are modeled by using subgrid momemtum and combustion models. In the current study, a spatial top hat Favre filter is applied to the Navier Stokes equations,with a kernel size equal to the grid spacing (Δx), and the Favre-filted LES equations are obtained with all subgrid unclosed terms explicitly identified. This filtering operation decomposes the flow variable (f) into resolved Favre filtered ($\tilde{f}$) and unresolved subgrid (f'') components. The Favre-filtered variavle $\tilde{f}$ is defined by:

$$\tilde{f} = \frac{\overline{\rho f}}{\overline{\rho}} \tag{39}$$

$$f = \tilde{f} + f'' \tag{40}$$

where ρ is the local fluid density.

The following Favre-filtered form of the Navier Stokes equations are solved in the

current study:

$$\begin{aligned}
\frac{\partial \overline{\rho}}{\partial t} + \frac{\partial \overline{\rho}\tilde{u}_i}{\partial x_i} &= 0 \\
\frac{\partial \overline{\rho}\tilde{u}_i}{\partial t} + \frac{\partial}{\partial x_j}[\overline{\rho}\tilde{u}_i\tilde{u}_j + \overline{p}\delta_{ij} - \overline{\tau}_{ij} + \tau_{ij}^{sgs}] &= 0 \\
\frac{\partial \overline{\rho}\tilde{E}}{\partial t} + \frac{\partial}{\partial x_i}[\left(\overline{\rho}\tilde{E} + \overline{p}\right)\widetilde{u}_i + \overline{q}_i - \tilde{u}_j\overline{\tau}_{ji} + H_i^{sgs} + \sigma_i^{sgs}] &= 0 \\
\frac{\partial \overline{\rho}\tilde{Y}_k}{\partial t} + \frac{\partial}{\partial x_i}[\overline{\rho}\tilde{Y}_k\tilde{u}_i + \overline{\rho}\widetilde{Y_k V_{i,k}} + \phi_{i.k}^{sgs} + \theta_{i,k}^{sgs}] &= \overline{\dot{\omega}}_k
\end{aligned} \tag{41}$$

In Eq.(41) the total energy E is defined as the sum of kinetic energy and internal energy, the Favre averaged total energy $\widetilde{E}$ is given by:

$$\tilde{E} = \tilde{e} + \frac{1}{2}\widetilde{u_k u_k} \tag{42}$$

$$= \tilde{e} + \frac{1}{2}\widetilde{u}_k\widetilde{u}_k + \frac{1}{2}\left(\widetilde{u_k u_k} - \tilde{u}_k\tilde{u}_k\right) \tag{43}$$

$$= \tilde{e} + \frac{1}{2}\widetilde{u}_k\widetilde{u}_k + k^{sgs} \tag{44}$$

where $\tilde{e}$ is the filtered internal energy and k^{sgs} is the unresolved or subgrid part of the kinetic energy. The filtered pressure is calculated as the filtered equation of state as[11]:

$$\overline{p} = \overline{\rho RT} = \overline{\rho}\widetilde{RT} \tag{45}$$

$$= \overline{\rho}\widetilde{R}\widetilde{T} + \overline{\rho}R_u T^{sgs} \tag{46}$$

where R is the mixtute gas constant. In the current study T^{sgs} is neglected. $\tilde{V_{i,k}}$ is filtered diffusion velocity of the k-th species and is given as:

$$\widetilde{V}_{i,k} = -\frac{\overline{D}_{km}}{\widetilde{X}_k}\frac{\partial \widetilde{X}_k}{\partial x_i} + \widetilde{V_i^C} \tag{47}$$

where $\overline{D}_{km}$ is the mixture averaged species diffusivity and $\tilde{V_i^C}$ is the correction velocity. The filtered heat flux vector is given by:

$$\overline{q}_i = -\overline{\kappa}\frac{\partial \widetilde{T}}{\partial x_i} + \overline{\rho}\sum_{k=1}^{N_s}\widetilde{h}_k\widetilde{Y}_k\widetilde{V}_{i,k} + \sum_{k=1}^{N_s} q_i^{sgs} \tag{48}$$

where $\tilde{h}_k$ and $\overline{\kappa}$ denote the Favre filtered k-th species enthalpy and thermal conductivity. All the subgrid-scale terms are denoted with sgs are unclosed and they need to be modeled. These terms are the subgrid shear stress $\left(\tau_{ij}^{sgs}\right)$, subgrid viscous work (H_i^{sgs}), subgrid viscous stress (σ_i^{sgs}), subgrid mass flux $\left(\phi_{i,k}^{sgs}\right)$, subgrid diffusive mass flux $\left(\theta_{i,k}^{sgs}\right)$, and subgrid heat transfer via turbulent convection of species $\left(q_{i,k}^{sgs}\right)$.The subgrid terms in details are represented as:

$$\begin{aligned}
\tau_{ij}^{sgs} &= \overline{\rho}\left(\widetilde{u_i u_j} - \widetilde{u}_i\widetilde{u}_j\right) \\
H_i^{sgs} &= \overline{\rho}\left(\widetilde{Eu_i} - \widetilde{E}\widetilde{u}_i\right) + \left(\overline{pu_i} - \overline{p}\widetilde{u}_i\right) \\
\sigma_i^{sgs} &= \left(\overline{u_j\tau_{ij}} - \widetilde{u}_j\overline{\tau}_{ij}\right) \\
\phi_{i,k}^{sgs} &= \overline{\rho}\left(\widetilde{Y_k u_i} - \widetilde{Y}_k\tilde{u}_i\right) \\
\theta_{i,k}^{sgs} &= \overline{\rho}\left(\widetilde{V_{i,k}Y_k} - \widetilde{V}_{i,k}\widetilde{Y}_k\right) \\
q_{i,k}^{sgs} &= \overline{\rho}\left(\widetilde{h_k Y_k V_{i,k}} - \widetilde{h}_k\widetilde{Y}_k\widetilde{V_{i,k}}\right)
\end{aligned} \tag{49}$$

The closure strategy to model the subgrid terms is presented in the next sections.

2.5.1 Subgrid Momentum Modeling

An eddy viscosity type closure is adopted for momentum and energy transport beacause the major effect of small scales is to provide dissipation to the enrgy budget of the flow. the eddy viscosity, ν_t, is evaluated using a characteristic length-scale, provided by the local grid size$\overline{\Delta}$ where $\overline{\Delta} = (\Delta_x\Delta_y\Delta_z)^{\frac{1}{3}}$, and a subgrid velocity, obtained from the subgrid kinetic energy k^{sgs}, so that $\nu_t = C_\nu\overline{\Delta}\sqrt{k^{sgs}}$.The subgrid momentum tensor is modeled as:

$$\tau_{ij}^{sgs} = -2\overline{\rho}\nu_t\left(\widetilde{S}_{ij} - \frac{1}{3}\widetilde{S}_{k,k}\delta_{ij}\right) + \frac{2}{3}\overline{\rho}k^{sgs}\delta_{ij} \tag{50}$$

where Pr_t is the turbulent Prandtl number ($Pr_t = 0.6$)[3]. The two unclosed terms in the energy equation, H_i^{sgs} and σ_i^{sgs} are modeled together as:

$$H_i^{sgs} + \sigma_i^{sgs} = -2\overline{\rho}\frac{\nu_t}{Pr_t}C_p\frac{\partial\widetilde{T}}{\partial\widetilde{x}_i} + \tau_{i,j}^{sgs}\widetilde{u}_i - \left(\rho\frac{\nu_t}{Pr_t} + \mu\right)\frac{\partial\widetilde{k}^{sgs}}{\partial x_i} \tag{51}$$

For closure an additional transport equation for the subgrid scale kinetic energy k^{sgs} is solved, which is in the form of:

$$\frac{\partial \overline{\rho} k^{sgs}}{\partial t} + \frac{\partial}{\partial x_i}\left(\overline{\rho}\widetilde{u}_i k^{sgs}\right) = P^{sgs} - D^{sgs} + \frac{\partial}{\partial x_i}\left(\frac{\overline{\rho}\nu_t}{Pr_t}\frac{\partial k^{sgs}}{\partial x_i}\right) \tag{52}$$

where $P^{sgs} = -\tau_{ij}^{sgs}\frac{\partial \widetilde{u}_i}{\partial \widetilde{x}_j}$, and $D^{sgs} = C_\epsilon \overline{\rho}\left(\widetilde{k}^{sgs}\right)^{\frac{3}{2}}/\overline{\Delta}$, are the production and the dissipation of the k^{sgs}, respectively. In this equation, $Pr_t = 1$, the two coefficients, C_ν and C_ϵ have constant value of 0.067 and 0.916, based on earlier calculations. The present study uses a dynamic approach (LDKM hereafter) to compute the model coefficients C_ν and C_ϵ, based on the assumption that the resolved and the unresolved small scales behave in a similar manner and hence the model coefficients can be computed from similarity relations[21, 22]. Based on experimental observations it was found that for high Reynolds number flows the subgrid stress $\left(\tau_{ij}^{sgs}\right)$ at the grid filter level $\overline{\Delta}$ and the Leonard's stress (L_{ij}) at the test filter level $\left(\hat{\Delta} = 2\overline{\Delta}\right)$ are self-similar. L_{ij} is given by the following expression:

$$L_{ij} = \langle \overline{\rho}\widetilde{u}_i\widetilde{u}_j\rangle - \left[\langle \overline{\rho}\widetilde{u}_i\rangle\langle \overline{\rho}\widetilde{u}_j\rangle\right]/\widehat{\overline{\rho}} \tag{53}$$

LDKM assumes that the sub-grid stress at the test filter level $\left(\widehat{\tau}_{ij}^{sgs}\right)$ are also similar $\left(\hat{\tau}_{ij}^{sgs} = \widehat{C}_L L_{ij}\right)$. Then $\widehat{\tau}_{ij}^{sgs}$ is modeled using the same form used for τ_{ij}^{sgs} with all variables defined at the test filter level. With this assumption the expression for L_{ij} becomes:

$$L_{ij} = \frac{\widehat{\tau}_{ij}^{sgs}}{\widehat{C}_L} = 2\widehat{\overline{\rho}}\frac{C_\nu}{\widehat{C}_L}\sqrt{k^{test}}\widehat{\Delta}\left(\left\langle \widetilde{S}_{ij}\right\rangle - \frac{1}{3}\left\langle \widetilde{S}_{kk}\right\rangle \delta_{ij}\right) + \frac{2}{3}\frac{1}{\widehat{C}_L}\widehat{\overline{\rho}}k^{test}\delta_{ij} \tag{54}$$

Assuming $\widehat{C}_L = 1$, C_ν is determined using the least square method of Lilly:

$$C_\nu = -\frac{L'_{ij}M_{ij}}{2M_{ij}M_{ij}} \tag{55}$$

In the above expression, $L'_{ij} = L_{ij} - \frac{2}{3}\widehat{\overline{\rho}}k^{test}\delta_{ij}$, and $M_{ij} = \widehat{\overline{\rho}}\sqrt{k^{test}}\widehat{\Delta}\left(\left\langle \widetilde{S}_{ij}\right\rangle - \frac{1}{3}\left\langle \widetilde{S}_{kk}\right\rangle \delta_{ij}\right)$. A similar approach is used to obtain the dissipation coefficient C_ϵ:

$$C_\epsilon = \frac{\widehat{\Delta}\left(\overline{\mu} + \mu_t\right)}{\widehat{\overline{\rho}}k^{test\,3/2}}\left[\left\langle \widetilde{T}_{ij}\frac{\partial \widetilde{u}_j}{\partial x_i}\right\rangle - \widehat{\widetilde{T}_{ij}}\widehat{\frac{\partial \widetilde{u}_j}{\partial x_i}}\right] \tag{56}$$

where, $\mu_t = \overline{\rho}\nu_t$, $\widetilde{T}_{ij} = \left[\frac{\partial \widetilde{u}_i}{\partial x_j} + \frac{\partial \widetilde{u}_j}{\partial x_i} - \frac{2}{3}\frac{\partial \widetilde{u}_k}{\partial x_k}\delta_{ij}\right]$, and $\widehat{\widetilde{T}}_{ij}$ is the stress tensor at the test filter level. Seven realizability conditions need to be satisfied for a subgrid scale stress tensor to guarantee a realizable solution. These conditions are:

(1-3) $\tau_{ij} \geq 0$, where $i = 1, 2, 3$;

(4-6) $|\tau_{ij}| \leq \sqrt{\tau_{ii}\tau_{jj}}$, where $i \neq j$;

(7) $\det(\tau_{ij}) \geq 0$.

The LDKM approach is ensured to satisfy all the realizability conditions at majority of grid points.

2.5.2 Subgrid Combustion Modelling using LEM

In the present study a subgrid combustion model based on LEM is used to account for the combustion occurring within the LES cells (LEMLES, hereafter), since combustion, heat release, volumetric expansion and small-scale turbulent stirring all occur at small scales, which are not resolved in a conventional LES approach. No explicit closure is provided for subgrid mass flux, $\phi_{i,k}^{sgs}$, the subgrid diffusive flux, $\theta_{i,k}^{sgs}$, and the filtered reaction rate $\overline{\dot{\omega}}_k$, since a more accurate and exact closure is implemented withinthe subgrid scales.

LEM is a stochastic, Monte-Carlo simulation of the unsteady scalar field evolution in a turbulent flow, based on solving the unsteady reaction-diffusion equation on a one-dimensional domain, treating turbulent convection separately at its own time scale. The computational domain is aligned in the direction of the steepest scalar gradient with grid resolution η. The turbulent field is assumed to be isotropic with no boundaries and/or body forces. In LEM, the molecular diffusion and chemical reaction evolve deterministically from an initial scalar field by the solution of the thermochemical equations.

Consider the following exact transport equation for the k-th scalar Y_k, where there is

no spatial filtering:

$$\rho\frac{\partial Y_k}{\partial t} = -\rho\left[\widetilde{u}_i + (u_i')^R + (u_i')^S\right]\frac{\partial Y_k}{\partial x_i} - \frac{\partial}{\partial x_i}\left(\rho Y_k\left(V_{i,k} + V_i^C\right)\right) + \dot{\omega}_k \tag{57}$$

The convective velocity is separated into three parts: the LES resolved velocity field $\widetilde{u}_i$, the LES resolved subgrid fluctuation (obtained from k^{sgs}) $(\widetilde{u}_i)^R$, and the unresolved subgrid fluctiation $(\widetilde{u}_i)^S$. Using this definition eq. (57) can be split into the following two-step numerical form:

$$\rho\frac{\partial Y_k}{\partial t} = -\left[(\widetilde{u}_i + u_i')^R\right]\frac{\partial Y_k}{\partial x_i} \tag{58}$$

$$\rho\frac{\partial Y_k}{\partial t} = \rho\,(u_i')^S\frac{\partial Y_k}{\partial x_i} + \frac{\partial}{\partial x_i}\left(\rho Y_k\left(V_{i,k} - V_i^C\right)\right) - \dot{\omega}_k \tag{59}$$

Eqs. (58) and (59) represent large-scale and small-scale processes, respectively. The large-scale step advects the subgrid scalar gradient using a 3D Lagrangian process that ensures strict mass conservation and preserves the small-scale scalar structure. In eq. (59) the three terms represent the small-scale turbulent stirring, molecular diffusion and chemical kinetics, respectively. Eq. (59) is solved on a 1D line embedded inside each LES cells with a subgrid resolution fine enough to resolve the Kolmogorov scale, η, so that both molecular diffusion and reaction rate are closed in an exact sense.

Based on this approach, in the LEMLES model the following reaction-diffusion equation is solved on the 1D LEM level:

$$\begin{aligned}\rho\frac{\partial Y_k}{\partial t} &= F_{k,stir} - \frac{\partial}{\partial s}\left(\rho Y_k\left(V_{k,s} - V_k^C\right)\right) + \dot{\omega}_k \\ \rho C_p\frac{\partial T}{\partial t} &= F_{T,stir} - \rho\frac{\partial T}{\partial s}\left(\sum_{k=1}^{N_s} C_{p,k}Y_k\left(V_{k,s} - V_s^C\right)\right) + \frac{\partial}{\partial s}\left(\kappa\frac{\partial T}{\partial s}\right) + \dot{\omega}_T\end{aligned} \tag{60}$$

In this equation, heat release due to combustion is calculated as $\dot{\omega}_T = -\sum_{k=1}^{N_s} h_k\dot{\omega}_k W_k$. The subgrid field within each LES supergrid is resolved by N_{LEM} number of cells along the local coordinate s, aligned in the direction of the steepest gradient.

2.5.2.1 Small Scales: Turbulent Stirring

Within LEM, turbulent stirring is solved stochastically by a numerical re-arrangement event known as triplet-maps, represented symbolically by $F_{k,stir}$ and $F_{T,stir}$ in Eq. (60). It is based on the assumption that the effect of the turbulent eddies on the scalar field is to stochastically redistribute the concentration gradients, by only increasing the scalar gradients. Hence, for a given initial scalar profile, the turbulent advection increases the gradients by re-distribution process whereas molecular diffusion competes with it by smoothing out these gradients. Schematically, this mapping first creates three copies of the selected segment by a factor of three and reversing the middle segment.

The location of stirring event is chosen randomly from a uniform distribution and the frequency of stirring is implemented as a Poison process in time [19] as:

$$\lambda = \frac{54}{5}\frac{\nu Re_{\bar{\Delta}}}{C_\lambda \bar{\Delta}^3}\frac{\left[\left(\frac{\bar{\Delta}}{\eta}\right)^{5/3} - 1\right]}{\left[1 - \left(\frac{\eta}{\bar{\Delta}}\right)^{4/3}\right]} \tag{61}$$

where, $C_\lambda = 0.067$ [5]. The eddy size (l) is picked randomly from an eddy distribution $f(l)$ ranging from $\bar{\Delta}$ to η:

$$f(l) = \frac{5}{3}\frac{l^{-8/3}}{(\eta^{-5/3} - \Delta^{-5/3})} \tag{62}$$

where $\eta = N_\eta \bar{\Delta} Re_{\bar{\Delta}}^{-3/4}$ and $Re_{\bar{\Delta}} = u'\bar{\Delta}/\nu$ is the subgrid Reynolds number.

2.5.2.2 Volumetric expansion

The volumetric expansion in LEM is implemented locally within the subgrid by expanding the LEM domain and after splicing re-griding is done to keep the total number of LEM constant within each cell.

2.5.2.3 Large Scales: Advection

After the evolution of the subgrid scalar field, large scale advection is implemented by a 3D Lagrangian process known as splicing that determines the amount of mass

to be advected and advects this amount with the subgrid scalar fields across the LES cell faces.

2.5.3 Subgrid Combustion Modelling directly within LES

In the LES simulation $\theta_{i,k}^{sgs}$ is neglected and the $\phi_{i,k}^{sgs}$ is modelled $\phi_{i,k}^{sgs} = -\frac{\overline{\rho}\nu_t}{Sc_t}\frac{\partial \widetilde{Y}_k}{\partial x_i}$. For the filtered reaction rate $\overline{\dot{\omega}}_k$ some form of closure is required. This closure is discussed in details later.

CHAPTER III

PROBLEM SETUP

Two cases corresponding to a low and a high Re, are chosen as test cases from the previous DNS study [14] of 3D turbulent temporally evolving syngas(CO/H_2)-air diffusion flames. These cases exhibit local extinction and reigintion as a result of strong flame-turbulence interaction and poses a challenging problem for the TANN methodology. Both the LES and DNS study employ the same setup.

3.1 Problem Description

The central fuel stream, of width H, is composed of 50% CO, 10% H_2 and 40% N_2 by volume. Surrounding the central fuel stream are counter-flowing oxidizer streams composed of 25% O_2 and 75% N_2. The domain size is $L_X = 12H$ in stream-wise direction, $L_Y = 14H$ in the transverse direction and $L_Z = 8H$ in the span-wise direction. The boundary conditions are periodic, non-reflecting outflow and periodic in the stream-wise, transverse and span-wise directions, respectively. The details of the two DNS cases are give in table 1.

The LES study employs grids clustered near the shear layer in the flame normal direction with smooth stretching towards the transverse boundaries, while uniform spacing is used in the other two directions because the gradients are highest across

Table 1: DNS parameters for test cases

Parameter	Case L	Case H
$H(mm)$	0.72	1.37
Re_{jet}	2510	9079
Grid Size (M)	148	500
Grid Resolution	0.83η	1.67η

Table 2: LES parameters for test cases

Grid Resolution	Size	min. Δy	max. Δy
Case L	$90 \times 126 \times 50$ $(0.56M)$	0.055 mm	0.152 mm
Case H (C-GRID)	$120 \times 180 \times 90$ $(1.9M)$	0.045 mm	0.218 mm
Case H (M-GRID)	$160 \times 240 \times 120$ $(4.6M)$	0.035 mm	0.161 mm
Case H (F-GRID)	$200 \times 300 \times 150$ $(9M)$	0.028 mm	0.129 mm

the flame in the flame normal direction. The details of the LES setup is given in table 2. Like the DNS study, the LES is initialized with a laminar flamelet solution at a scalar dissipation rate $\chi = 0.75\chi_q$ ($\chi_q = 2194s^{-1}$, extinction scalar dissipation rate). For calculating the heat and species diffusion fluxes mixture-averaged transport properties are used.

CHAPTER IV

RESULTS

4.1 ANN Net Generation

One LANN net and three TANN nets: TANN-1, TANN-2 and TANN-3 are generated. Training data for LANN and TANN-1 is generated from a 1D stand-alone LEM simulation (Stand-alone LEM 1). Training data for TANN-2 and TANN-3 is generated from another stand-alone simulation run over a larger range of Re_t (Stand-alone LEM 2). Both the standalone LEM simulations are initialized with the same OPPDIFF flame obtained from Chemkin.

Stand-alone LEM 1 is simulated for Re_t up to 1000. Instantaneous thermochemical data is tabulated at regular intervals for generating the training table for LANN. For generating the training table for TANN-1, the data on the 1D stand-alone LEM domain is filtered over a fixed filter size of 0.1 mm and time step size of $2.5 \times 10^{-8} s$. The filter size and time step size is representative of the Case L LES grid size and time step size. In order to generate TANN capable of handling a larger range of χ, stand-alone LEM 2 is simulated for Re_t up to 1500. A fixed filter size of 0.042 mm and time step size of $1.0 \times 10^{-8} s$ are chosen to generate the training table for TANN-2. The filter size is representative of the average grid size for all the four LES cases and the time step size is smaller than the time step size for finest LES grid. This time step size is enforced for all LES simulations while using TANN-2 and TANN-3. For generating the training table for TANN-3, the training table for TANN-2 is re-tabulated with the species dissipation rate instead of species gradient.

For training the ANN nets, the training data is split into two tables Train and Test. The Train table gets 80% of the data and Test table gets 20%. The data in the Train

table is used for training the net. Once the training is complete, data in the Test table is used for comparing the source term obtained from ANN with the source term tabulated from the stand-alone LEM simulation. This gives an estimate about how the ANN net will perform at thermochemical data points for which it has not been trained.

Choosing the ANN architecture with the correct number of hidden layers and number of processing elements in each hidden layer is a challenging task. Two or more number of hidden layers is required for modelling complex data with discontinuities. If an inadequate number of processing elements are used in a hidden layer, the net will not be able to model complex data. On the other hand, if too many neurons are used, training time will become excessively long and the model may memorize the data. This result in ANN net fitting the data for which it is trained extremely well but generalizing poorly to new unseen data. In the present study all the 4 nets are trained with 3 hidden layers. The LANN is trained with 5, 4 and 3 processing elements in 1st, 2nd and 3rd hidden layers. The LANN has 12 processing elements in the input layer, 1 for the each of the 11 species ($H_2, O_2, OH, O, H_2O, H, HO_2, CO, CO_2, HCO, N_2$) and the 12th for temperature. Since, pressure is a constant in the present study; it is not used as an input. The TANN nets are trained with 10, 8 and 4 processing elements in the 1st, 2nd and 3rd hidden layers. The TANN input layer has 14 processing elements in the input layer, 11 for the species, 12th for the temperature, 13th for turbulent Re and the last one for species gradient in case of TANN-1 and TANN-2, and species dissipation rate for TANN-3. These architectures are chosen based on a previous study[32]. To prevent memorization of data by the ANN, it is necessary to stop the training at the correct time, once the training error does not change significantly with further iterations. In the present study, the training is stopped if the training error does not decrease after a given number of iterations.

4.2 Verification of the accuracy of the nets

After the training of the ANN net is complete and the weight distribution is optimum, to verify the accuracy of the network, the target values for the source term from the Test table are compared with the values predicted by the ANN network. Fig. 4 shows the comparison of the Target values and ANN predicted values for TANN-2 net. All the data points would have fallen on red line had the training been perfect. It is observed that there is some deviation from the red line. Most points show very little deviation from the red line and very few points show large deviation from the red line. Overall, TANN-2 predicts ANN values very close to target values for most of the test data points and the training is good. Similar trends are observed for the Target vs. ANN predicted values for other nets. Hence, all the four ANN nets are trained well.

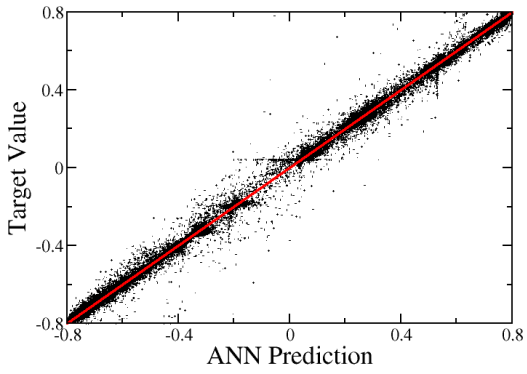

Figure 4: Comparison of Target vs. ANN prediction using TANN-2

4.3 Difference between LANN and TANN

The LANN is capable of calculating the instantaneous source terms within the LEM subgrid combustion model in LES framework as:

$$\frac{\dot{\omega}_i}{\rho} = f\left(Y_1, ..., Y_{N_s}, T\right) \text{ where, i=1,....,} N_s \tag{63}$$

for a fixed Δt and pressure.

TANN-1 and TANN-2 can compute the filtered source terms directly within the LES framework as:

$$\frac{\overline{\dot{\omega}}_i}{\overline{\rho}} = f\left(\widetilde{Y}_1, ..., \widetilde{Y}_{N_s}, \widetilde{T}, Re_\Delta, \frac{\partial \widetilde{Y}_i}{\partial x_j}\right) \text{ where, i=1,....,} N_s \tag{64}$$

for a fixed Δt, pressure and filter size representative of LES grid size.

TANN-3 can compute the filtered source terms directly within the LES framework as:

$$\frac{\overline{\dot{\omega}}_i}{\overline{\rho}} = f\left(\widetilde{Y}_1, ..., \widetilde{Y}_{N_s}, \widetilde{T}, Re_\Delta, 2D_i \frac{\partial \widetilde{Y}_i}{\partial x_j}.\frac{\partial \widetilde{Y}_i}{\partial x_j}\right) \text{ where, i=1,....,} N_s \tag{65}$$

for a fixed Δt, pressure and filter size representative of LES grid size.

The TANNs are trained as a function of the subgrid Re and filtered species gradient or filtered species dissipation rate, in addition to the filtered species mass fractions and filtered temperature. This is done to take into account the effect of turbulence and subgrid mixing. To evaluate if there is any difference between the laminar (instantaneous) reaction rates and the filtered (turbulent) reaction rates, filtered reaction rates obtained from the stand-alone LEM are compared with the instantaneous reaction rates for the same composition and time step size, as shown in Fig. 5. To obtain the filtered reaction rates, the filtered mass fractions are calculated at a given instant of time and at an instant after the LES time step size, on the standalone LEM domain. Their difference divided by the LES time step size gives the filtered reaction rate. To compute the instantaneous reaction rate, the instantaneous mass fractions and temperature are taken as input. Then direct integration is used to compute the instantaneous reaction rates. It is observed that the production of CO_2 and the consumption of O_2 and CO is faster for laminar chemistry compared to the turbulent chemistry. For OH radical, the magnitude of the laminar reaction rates is much higher, compared to the filtered reaction rate. The other radicals also show

similar trend like OH. OH laminar reaction rates vary from -800 to +800, approximately and OH filtered reaction rates varies from -200 to +200, approximately. This indicates that OH radicals are produced and consumed at almost the same rate in a given chemistry. This keeps their concentration low. However, their rate of production and consumption with laminar chemistry is higher than turbulent chemistry. Overall, the laminar chemistry assumption predicts faster combustion compared to the turbulent chemistry because the laminar chemistry does not take into account the effect of turbulence and the high scalar dissipation rates, which leads to fast removal of heat and the radicals from the reaction zone and thus drop in the heat release rate.

Fig. 6(a) and 6(b) show the comparison between filtered reaction rate and the

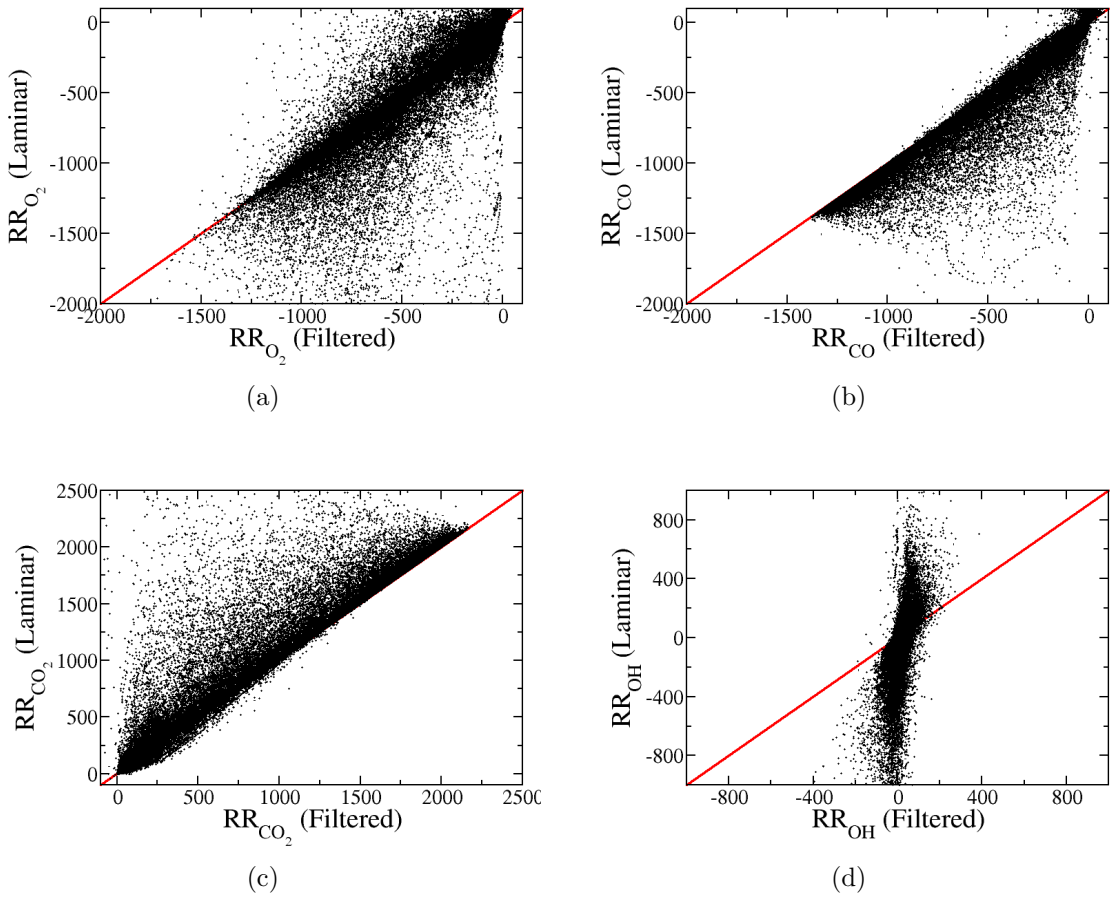

Figure 5: Comparison of the filtered reaction rates and the laminar reaction rates for (a) O_2, (b) CO, (c) CO_2, (d) OH.

laminar reaction rate of O_2 for low and high scalar dissipation rates. More difference between the laminar reaction rate and the filtered reaction rate is observed for higher scalar dissipation rates due to stronger turbulence-chemistry interactions which leads to to chemical time scales comparable with the diffusion time scales and thus laminar chemistry assumption is no longer valid. Hence, the source term predicted by LANN used directly within the LES framework is different from the source term predicted by TANN used within the LES framework.

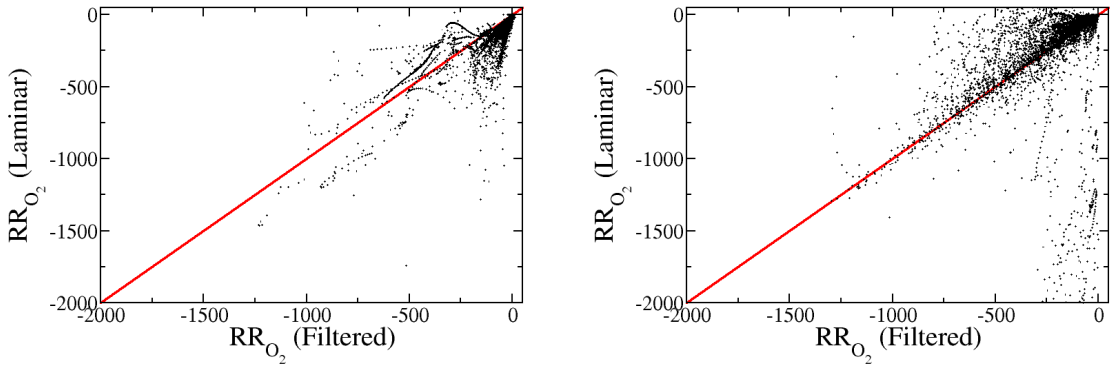

Figure 6: Comparison of the filtered reaction rates and the laminar reaction rates for O_2 at (a) $\chi < 1.0s^{-1}$, (b) $\chi > 1000s^{-1}$.

4.4 Comparison of TANN-1 and TANN-2 training data

Fig. 7(a) shows the comparison of χ with respect to Z for the standalone LEM data tables used for training the two nets TANN-1 and TANN-2. The standalone LEM data used for training TANN-1 was generated using a lower Re_t and larger filtered grid spacing compared to TANN-2 as explained in the previous section. As a result of higher Re_t and smaller grid spacing used for training TANN-2 compared to TANN-1, the χ values for TANN-2 are much higher. The TANN-1 and TANN-2 training data explore a maximum χ close to 20,000 and 50,000, respectively. Fig. 7(b) shows the

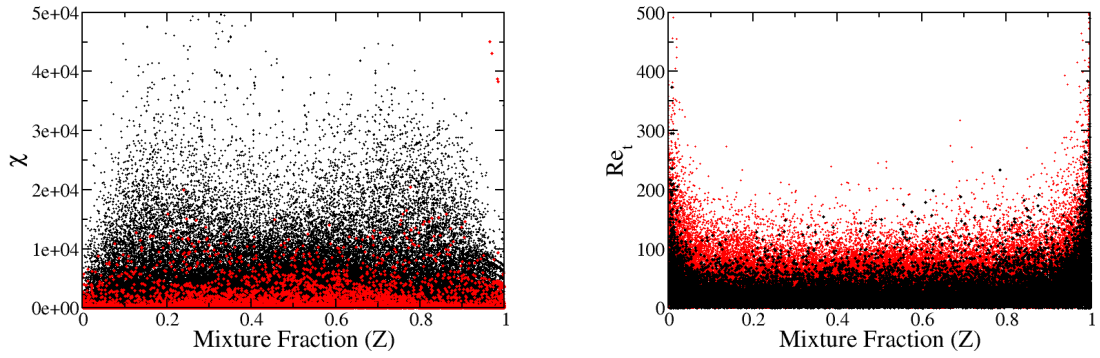

(a) (b)

Figure 7: Comparison of the standalone LEM data used for training the nets. Red symbols: TANN-1, Black symbols: TANN-2. (a) χ vs Z, (b) Re_t vs Z

comparison of Re_t with respect to Z for the two training data tables. It is observed that the Re_t values explored by TANN-1 are slightly higher than the Re_t values explored by TANN-2 because Re_t is directly proportional to the grid spacing and the grid spacing for TANN-2 is lower than the grid spacing for TANN-1.

Fig. 8(a) and 8(b) show the comparison of mass fraction of H_2 and OH with respect to temperature for the two training tables. The thermochemical data space covered by mass fraction of H_2, for the two training tables are very similar and overlap with each other. However, the thermochemical data space of OH does not overlap very well beyond a mass fraction of 2.5×10^{-3}. It is shown in the discussions later that the maximum OH mass fraction covered by the two LES test cases is around 2.5×10^{-3}. Hence, the region of mismatch for the OH thermochemical data space lies outside the area of interest for the two test cases. Therefore, based on the comparison of the training data for the two nets it is observed that even though the compositional data space explored by the two training tables are the same, the χ and Re_t data space differ. Hence, TANN-2 covers a wider range of χ compared to TANN-1 and is a more "generalized" net.

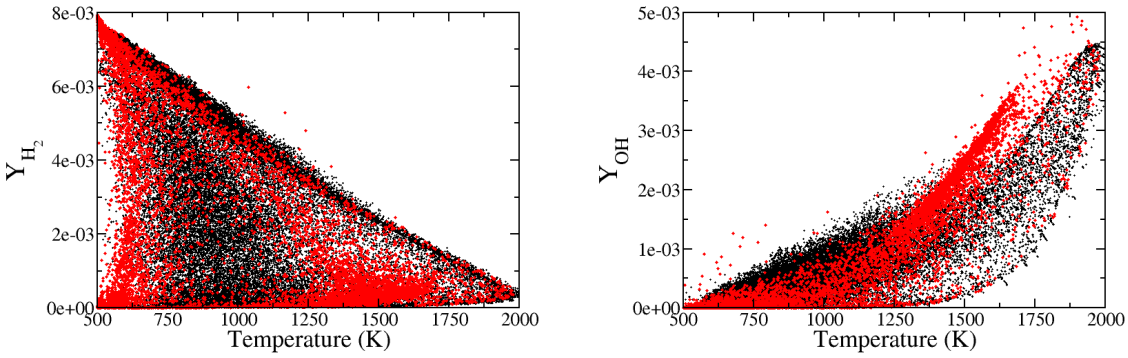

(a) (b)

Figure 8: Comparison of the standalone LEM data used for training the nets. Red symbols: TANN-1, Black symbols: TANN-2. (a) H_2 mass fraction vs Z, (b) OH mass fraction vs Z

4.5 Comparison of TANN-2 and TANN-3

TANN-2 and TANN-3 nets are trained on the same stand-alone LEM data. The only difference between the nets is TANN-2 computes the filtered source term as a function of species gradient whereas TANN-3 computes the source term as a function of species dissipation rate. The species dissipation rate is a function of the molecular diffusivity D in addition to species gradient and it plays an important role when the species in the reaction zone have a large range of molecular diffusivity. The lighter species like H, H_2 have higher molecular diffusivity than heavier species like CO, CO_2. Hence, for the same species gradient lighter species have a higher species dissipation rate compared to heavier species. Thus, TANN-3 takes into account the effect of variable species diffusivity in addition to the species gradient.

4.6 Case L: TANN-LES validation

To assess the performance of TANN methodology, the Case L is run with DI-LEMLES, LANN-LEMLES and TANN-LES using the TANN-1. Fig. 9(a) shows the variation of the mean temperature on the stoichiometric plane with respect to the non-dimensioned-time (t_j) for DNS, DI-LEMLES, LANN-LEMLES and TANN-LES. The time is non-dimensioned by the reference time obtained as $t^* = H/U$, where U is the already defined characteristic jet velocity [14]. The DNS data shows that the temperature begins at 1455 K and drops off to a minimum of approximately 1210 K near $t_j = 20$, indicating extinction. Beyond this point the temperature starts increasing again and reaches 1425 K at $t_j = 40$, showing complete reignition. The DI-LEMLES initially over predicts the temperature till $t_j = 10$ beyond which it drops off faster than the DNS temperature profile. LANN-LEMLES and TANN-LES almost at all instants till $t_j = 20$ under predict the mean temperature. The DI-LEMLES, LANN-LEMLES under predict the temperature by approximately 12% and the TANN-LES under predicts the temperature by approximately 8% at $t_j = 20$, indicating more extinction compared to DNS. Beyond this point, the temperature on the stoichiometric plane for DI-LEMLES and LANN-LEMLES increases at a higher rate compared to DNS temperature profile, while the TANN-LES stoichiometric plane temperature always remains lower than the DNS. At $t_j = 40$ the DI-LEMLES, LANN-LEMLES over predict the temperature by approximately 6% and TANN-LES under predicts the temperature by approximately 4%. The LES results highly under predict the temperature on the stoichiometric plane compared to DNS. In DNS, isotropic turbulence is added in the shear layer along a thickness lesser than the minimum LES grid size. Hence, when isotropic turbulence is added in the shear layer in LES it is done along a larger thickness.

Fig. 9(b) shows the variation of the mean χ_{st}/χ_q on the stoichiometric plane with respect to t_j. The DNS simulations initializes at $\chi_{st}/\chi_q = 0.75$ (approx.) and increases

to 2.16 at $t_j = 16$ due to the shear generated turbulence. Beyond this point it starts decaying and drops off to 0.35 at $t_j = 40$.

Comparing Fig. 9(a) and 9(b) it is observed that the local extinction is due to the

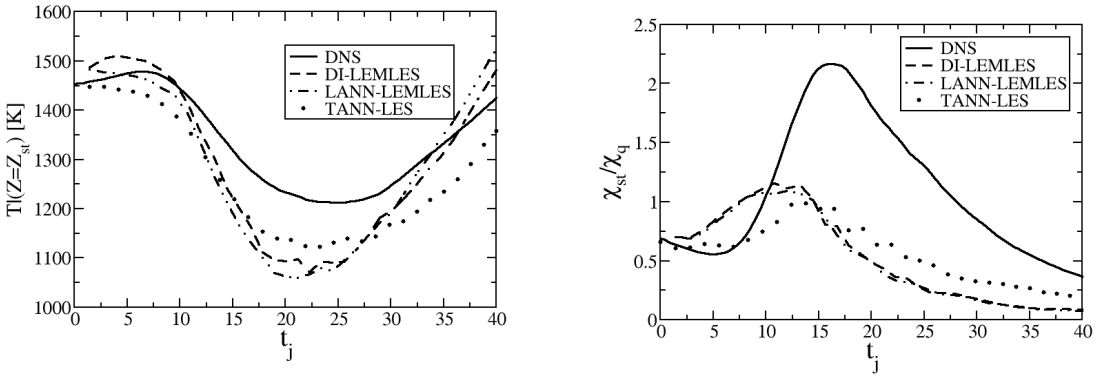

(a) (b)

Figure 9: (a) Variation of the mean of temperature at stoichiometric mixture fraction with respect to non-dimensional time for Case L, (b) Variation of the mean χ/χ_q at stoichiometric mixture fraction with respect to non-dimensional time for Case L

fluctuations of the scalar dissipation rate. Once the molecular mixing overcomes the effect of turbulent straining, it leads to the decrease of the scalar gradients which is accompanied by gradual reignition [37]. A time lag is observed between the maximum χ_{st}/χ_q and the minimum temperature on the stoichiometric plane because the reaction rate does not immediately follow variations of χ_{st} due to the finite rate chemistry [38],[26]. The temperature, at extinction is under predicted by 150K compared to DNS even though χ_{st} for LES is lower than the DNS by 100%. The reason the scalar dissipation is so much lower is LES is because it is using a much coarser grid and as Fig. 3 shows the gradient of Z appear lower on the filtered grid because it is not showing the subgrid fluctuations. So a coarser grid will always show a scalar dissipation rate lower than a fine-grid even though it takes into account the subgrid fluctuations in LEM or by computing the source term as a function of the gradient of the species at filtered level. The DI-LEMLES and LANN-LEMLES predict a faster

initial rate of growth of mean χ_{st}/χ_q compared to the DNS, while the TANN-LES predicts a slower initial rate of growth of χ_{st}/χ_q. The maximum mean χ_{st}/χ_q observed is approximately 1.1 and close to $t_j = 12$ for DI-LEMLES and LANN-LEMLES, while the maximum mean χ_{st}/χ_q for TANN-LES is observed close to $t_j = 15$ and has a value of 1 approximately. Beyond this point χ_{st}/χ_q decays off and reaches a value less than 0.2 at $tj = 40$ for DI-LEMLES and LANN-LEMLES, while it has a value of 0.25 approximately for TANN-LES. The TANN-LES under predicts χ_{st}/χ_q compared to LEMLES till $t_j = 15$ and after that it slightly over predicts. Overall the data obtained from TANN-LES is in good agreement with DI-LEMLES data. A similar assessment of case M having $Re = 4478$ [14] was done in an earlier study [32] and not shown here.

The mean value of temperature and H_2O mass fraction conditioned on the mixture fraction at extinction ($t_j = 20$) and reignition ($t_j = 40$) are shown in Fig. 10, with DNS, DI-LEMLES, LANN-LEMLES and TANN-LES using TANN-1. At extinction $t_j = 20$, the LES results under predict the mean temperature at almost all values of Z compared to the DNS. Above $Z = 0.95$ TANN-LES slightly over predicts the mean temperature. Overall, the TANN-LES mean temperature profile shows good match with the DNS temperature profile. Both LES and DNS show that the maximum value of Z observed for DI-LEMLES and LANN-LEMLES is 0.93. For TANN-LES the maximum value of Z observed is 0.975 and for DNS it is 0.97. Thus, DI-LEMLES and LANN-LEMLES overpredict mixing while TANN-LES slightly under predict it because of neglecting the subgrid diffusion term, compared to DNS, at extinction. A similar trend in mixture fraction is observed at reignition $t_j = 40$ and the maximum value of Z for DNS drops to 0.83. DI-LEMLES and LANN-LEMLES over predicts the mean temperature profile whereas TANN-LES under predicts the temperature profile at almost all values of Z, at reignition.The maximum temperature at both $t_j = 20$ and $t_j = 40$ is observed on the fuel-rich side instead of stoichiometric plane.

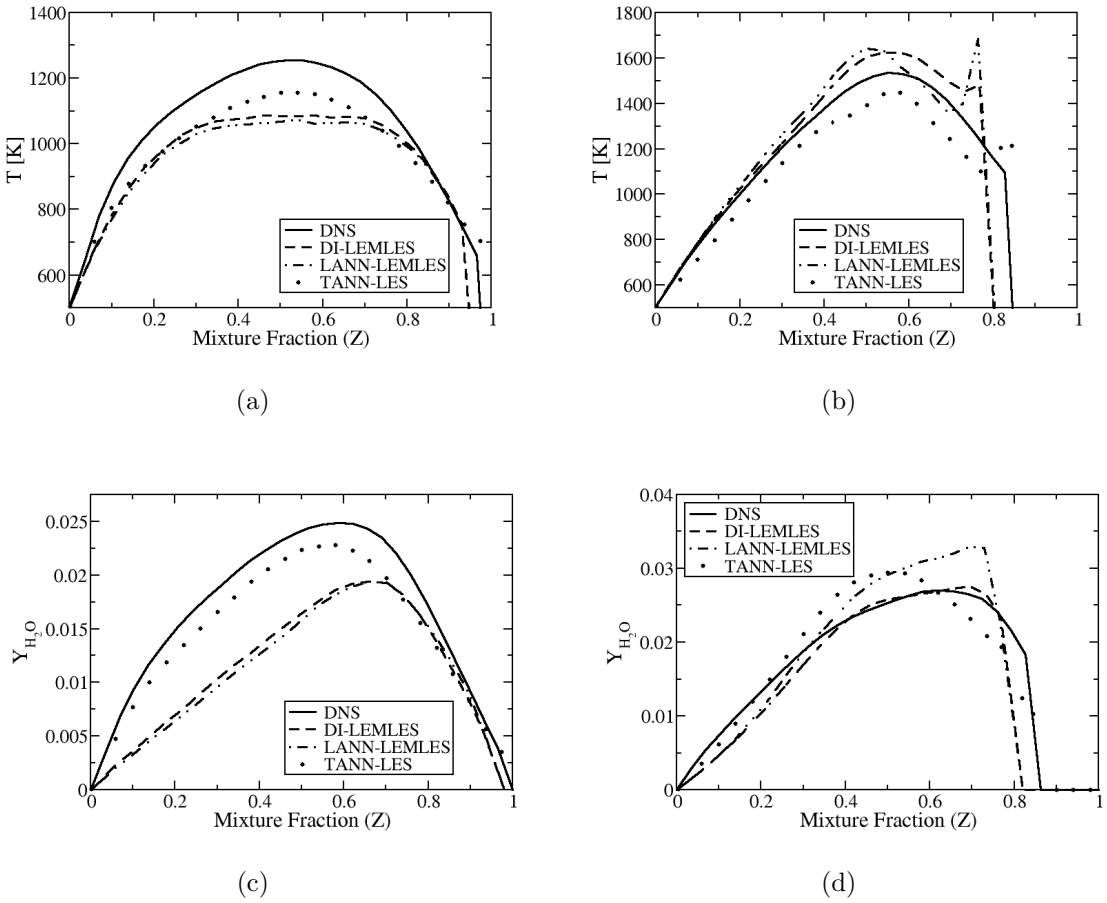

Figure 10: Conditional mean of temperature and Y_{H_2O} at extinction (a and c) and reignition (b and d)

This is observed due to the significant differential diffusion effect which leads to higher diffusion velocities of lighter species like H, H_2 OH and O compared to other species. The radicals diffuse more towards the fuel side and shift the location of the maximum heat release also making the heat release zone wider [15]. At extinction, the H_2O mass fraction is under predicted for all values of Z by the LES simulations. DI-LEMLES and LANN-LEMLES under predicts the production of H_2O more whereas TANN-LES under predicts it less compared to the DNS, which is consistent with the temperature profile predictions suggesting more extinction compared to the DNS and thus lower heat release rate and less production of products. The location of the maximum mass fraction of H_2O lies in the fuel-rich side, around 0.6 for DNS and TANN-LES and

around 0.7 for DI-LEMLES and LANN-LEMLES due to differential diffusion effects. The DNS data shows that maximum mass fraction of H_2O increases from 0.025 to 0.027 at $t_j = 20$ to $t_j = 40$. The LES results over predict the maximum mass fraction of H_2O at reignition compared to DNS.

Fig. 11 shows the time evolution of the scatter cloud of temperature with respect

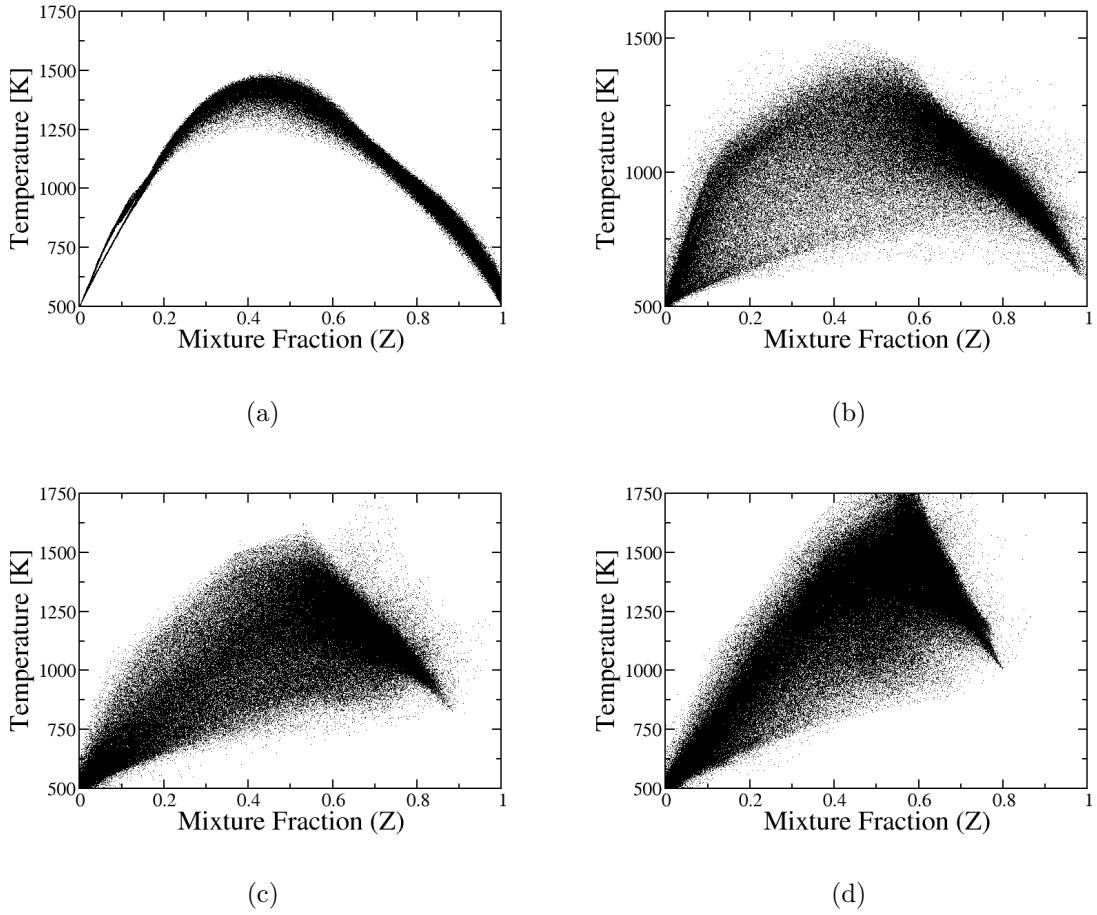

Figure 11: Case L, TANN-LES using TANN-1: Evolution of temperature w.r.t. Z at t_j a)10, b)20, c)30 and d)40.

to mixture fraction. At $t_j = 10$ a small scatter about the mean is observed. By $t_j = 20$ the scatter increases along with a drop in the mean temperature. At $t_j = 30$ and $t_j = 40$ the scatter reduces along with an upward shift of the cloud. The initial increase in the scatter and drop in the mean stoichiometric plane temperature at $t_j = 20$ followed by decrease in scatter and upward shift of the cloud at $t_j = 40$

indicates the extinction-reignition phenomenon.

Fig. 12(a) and 12(b) show the pdf of the H_2O and OH mass fraction at extinction

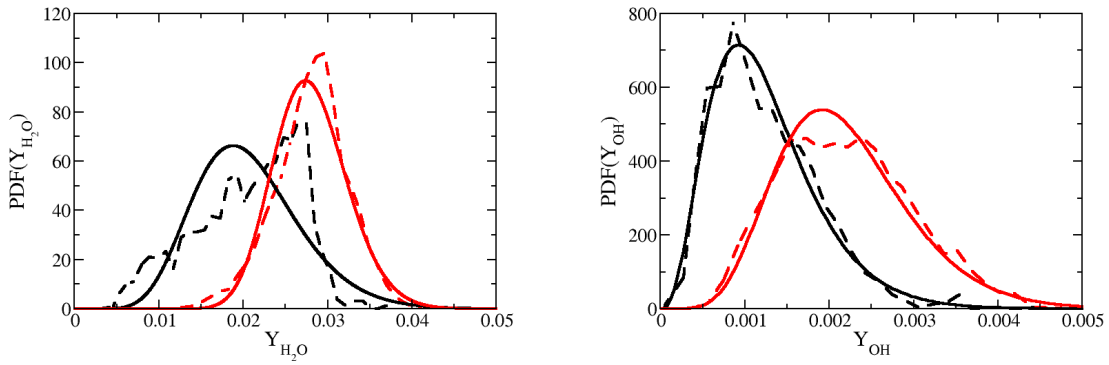

(a) (b)

Figure 12: Case L, TANN-LES using TANN-1: pdf on stoichiometric plane at extinction and reignition of a) H_2O, b) OH. Black continuous line: extinction($t_j = 20$), black broken line: β-pdf at extinction, red continuous line: reignition($t_j = 40$), red broken line: β-pdf at reignition,

($t_j = 20$) and reignition ($t_j = 40$) for TANN-LES using TANN-1. The pdf of H_2O shows more deviation from the beta-pdf at extinction than at reignition. This is in agreement with the observations made by Goldin et al. [13],[12] Near extinction due to the large values of χ on the stoichiometric plane the rate of diffusion of species is comparable with the chemical reaction rates resulting in high levels of chemical non-equilibrium which leads to scalar field deviation from the beta-pdf. At $t_j = 40$, once the mean χ_{st} has dropped off the system once again approaches chemical equilibrium and the pdf shows good agreement with the beta-pdf. The OH pdf matches well with the beta-pdf at both extinction and reignition because the chemical time scales of OH radical is small and hence OH mass fraction stays close to equilibrium at both extinction and reignition.

From the above studies it is concluded that the TANN-LES is a robust methodology and the results predicted by it compare well with the DNS, DI-LEMLES and LANN-LEMLES predictions. For all the results reported hereafter only TANN-LES

computations were done.

To show that TANN-2 (which is more "generalized" compared to TANN-1) is capable of handling a range of Re, case L is simulated with TANN-LES using TANN-2. Fig. 13(a) and 13(b) show the comparison of the temporal variation of mean temperature and mean χ_{st}/χ_q on the stoichiometric plane for case L using TANN-1 and TANN-2. Both TANN-1 and TANN-2 under predict the temperature on the stoichio-

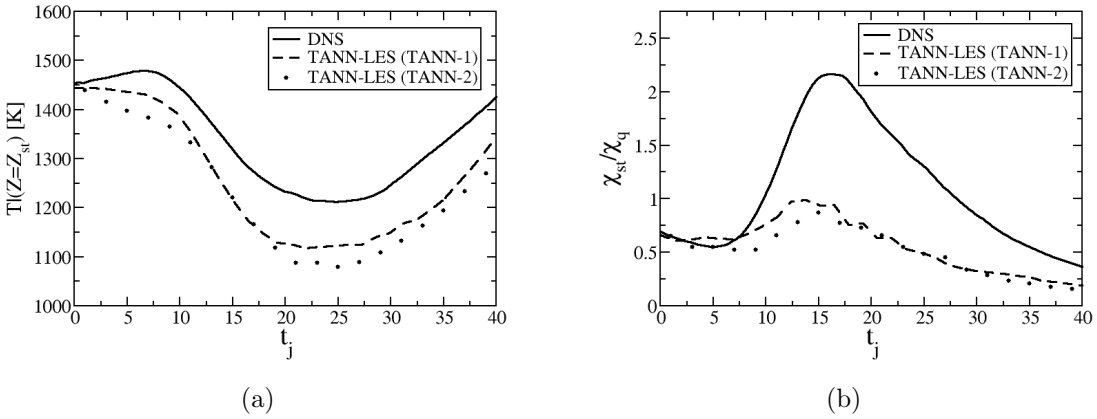

Figure 13: Comparison of the variation of (a) mean temperature and (b) mean χ/χ_q on the stoichiometric plane for Case L using TANN-1 and TANN-2

metric plane throughout the course of the simulation. TANN-1, trained on a smaller range of Re_t and grid-size matching with case L predicts a solution closer to DNS compared to TANN-2, trained on a wider range of Re_t and smaller grid spacing. The mean χ_{st}/χ_q is slightly under predicted by TANN-2 compared to TANN-1 till $t_j = 15$, beyond which the TANN-1 results almost overlap with TANN-2 results. Overall the TANN-1 and TANN-2 results match well for case L and loss of accuracy by using the generalized net TANN-2 compared to the case specific net TANN-1 is negligible.

4.7 Case H: Grid independence study using a single TANN net

The TANN-1 failed to predict extinction-reignition for Case H. TANN-2 generated for a larger range of Re_t as mentioned earlier successfully simulated Case H.

Fig. 14(a) and 14(b) show the variation of the mean temperature and mean χ_{st}/χ_q on the stoichiometric plane with respect to t_j for DNS and TANN-LES using TANN-2 for Case H C-GRID, M-GRID and F-GRID. Variation in the grid refinement results in F-GRID estimating the highest mean χ_{st}/χ_q and the C-GRID the lowest because a finer grid captures the subgrid fluctuations better. All the grids for case H predict the highest mean χ_{st}/χ_q around $t_j = 12$ which is slightly later in time compared to the prediction of DNS. After $t_j = 15$ the temperature field is slightly under predicted by all the three grids compared to the DNS data. Like DNS the extinction and reignition are observed at $t_j = 25$ and $t_j = 50$, respectively, even though the temperature at extinction is slightly under predicted. The lower mean temperature at extinction and longer reignition time, in case H compared to case L, is observed due to the higher levels of initial turbulence [14]. Overall, the mean temperature predictions for the three grids are reasonably consistent and compare well with the DNS data. Unlike Case L, the temperature on stoichiometric plane compare well for Case H C-GRID. Because the LES cell thickness size in shear layer for Case H C-GRID is smaller than Case L and in Case H, isotropic turbulence is added over a larger thickness. Hence, there is lesser mismatch in isotropic turbulence addition between DNS and LES in Case H compared to Case L.

Fig. 15 show the comparison of the pdfs of temperature, H_2O and OH mass fractions at extinction($t_j = 25$) and reignition($t_j = 50$) on the stoichiometric plane for C-GRID, M-GRID, F-GRID. The pdf profile of temperature at $t_j = 25$ for all the three grids compare well with each other having the mean around 900K with slight narrowing of the pdf from C-GRID to F-GRID. At $t_j = 50$ the mean of all the three pdfs shift

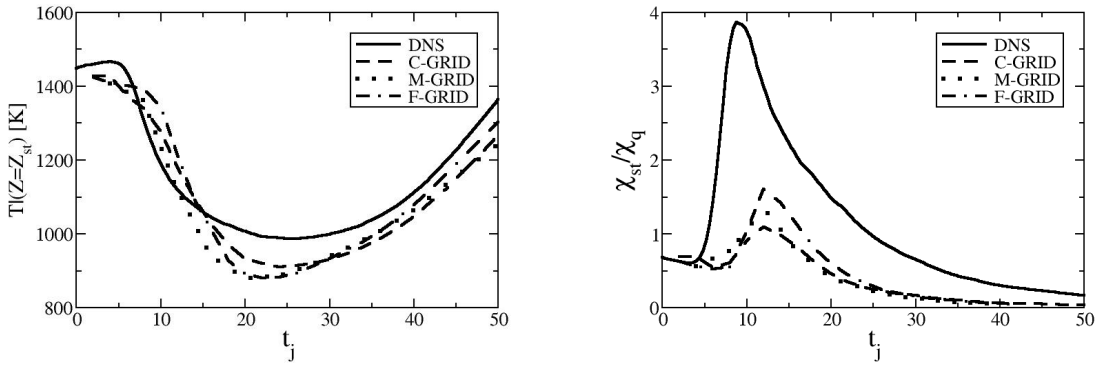

Figure 14: Case H (a) Variation of the mean of temperature at stoichiometric mixture fraction with respect to non-dimensional time, (b) Variation of the mean χ/χ_q at stoichiometric mixture fraction with respect to non-dimensional time

to 1300K with the low temperature tail subsiding. The F-GRID exhibits a more prominent low temperature tail suggesting the presence of more reignition compared to the other two cases. At $t_j = 25$, the pdf of the mass fraction of both H_2O and OH compare well with each other and the mean lie around 0.012 and 0.0004 for H_2O and OH respectively. At $t_j = 50$ the H_2O pdf narrows down and the mean H_2O and OH increases to 0.02 and 0.0012, respectively. Hence, these pdfs clearly exhibit the extinction-reignition process.

Fig. 16(a) and 16(b) show the comparison of the pdf of the normalized χ_{st} at different instants of time for C-GRID and F-GRID, respectively. Maximum negative skewness is observed at $t_j = 10$ where the mean χ_{st} is maximum for both the cases. The negative skewness is observed because at high values of mean χ_{st} only at very limited number of points on the stoichiometric plane the χ reaches very high values and shift the mean. At majority of the points on the stoichiometric plane the χ values lie below the mean and hence result in negative skewness. This phenomenon is explained in Fig. 17(a) and 17(b), which show the distribution of χ with respect to temperature on the stoichiometric plane for C-GRID and F-GRID, respectively. At $t_j = 10$ maximum points lie below mean χ_{st} value of 2000 and 2300 for C-GRID and

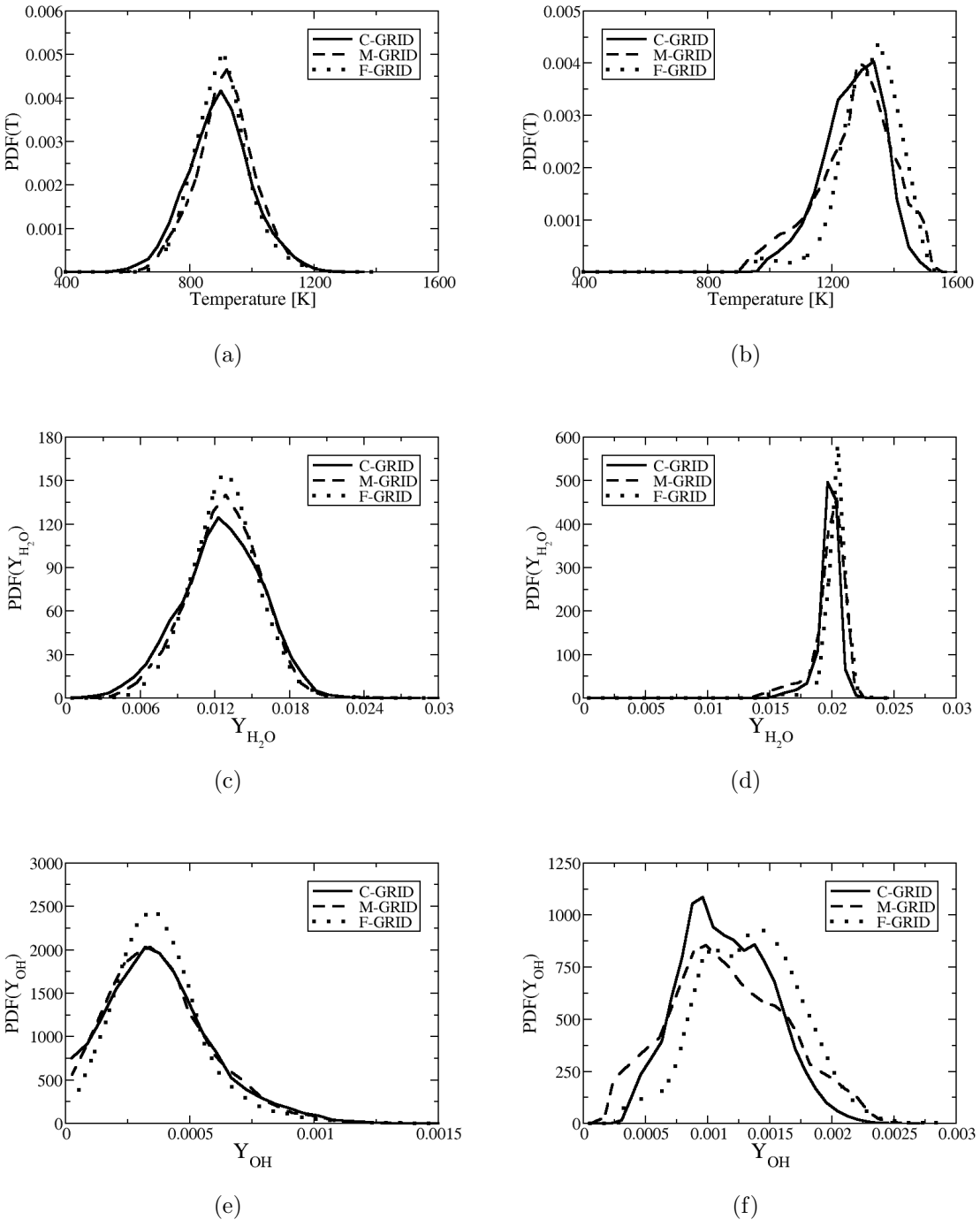

Figure 15: Variation of PDF of temperature, H_2O and OH mass fraction on stoichiometric plane at extinction: (a),(c),(e) and reignition: (b),(d),(f) for Case H with TANN-2

F-GRID, respectively. A very small fraction of points lie above this mean and has χ_{st} values as high as 4 times and 8 times greater than mean χ_{st} for C-GRID and F-GRID,

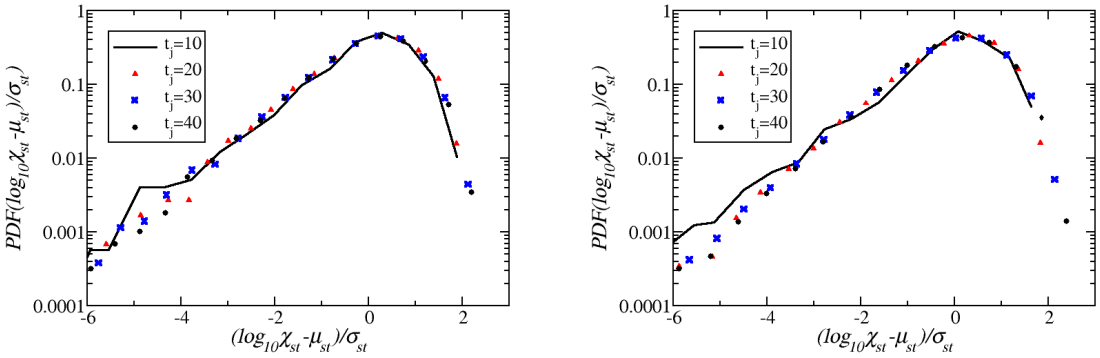

Figure 16: PDF of the normalized scalar dissipation rate at the stoichiometric mixture for Case H with TANN-2. (a) C-Grid, (b) F-Grid

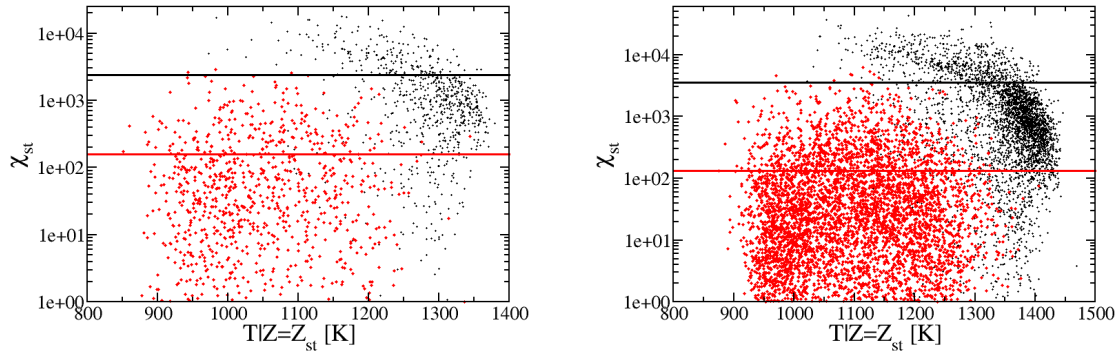

Figure 17: Distribution of χ_{st} with respect to temperature on the stoichiometric plane for Case H. Black dots: $t_j = 10$, Red dots: $t_j = 40$ for (a) C-GRID, (b) F-GRID

respectively. It is also observed that at extinction points with χ_{st} values above the mean $\chi_s t$ lie at lower temperatures indicating the formation of extinguished regions [36]. At $t_j = 40$ the stoichiometric data is spread over a wider range of temperature compared to the stoichiometric data at $t_j = 10$ and it is spread more uniformly about a lower mean of χ_{st} of 130 and 160 for C-GRID and F-GRID, respectively, which indicates partial reignition. This results in less negative skewness. Further it is observed that at $t_j = 10$ the stoichiometric data is more clustered below $\chi_{st} = 2000$ for

F-GRID compared to C-GRID. This has lead to the smoother normalized χ_{st} profile for F-GRID compared to C-GRID at normalized χ_{st} values less than -3. Similar to $t_j = 40$ at $t_j = 20$ and $t_j = 30$, the mean χ_{st} is low and hence the negative skewness is not observed. Overall, the pdf of normalized χ_{st} for C-GRID and F-GRID are in good agreement.

Fig. 18(a) and 18(b) show the evolution of temperature and χ pdf on stoichiometric plane with time for case H M-GRID. The temperature pdf shifts rapidly to lower mean value and the variance increases going form $t_j = 10$ to $t_j = 20$. By $t_j = 30$ the variance decreases and with further increase in time the temperature pdf shifts to higher values. The χ pdf shifts to lower values with time. These results show that the TANN-2 is capable of capturing the complex extinction-reignition phenomenon and also handling grids of different resolutions. Fig. 19(a) and 19(b) show the χ vs Z

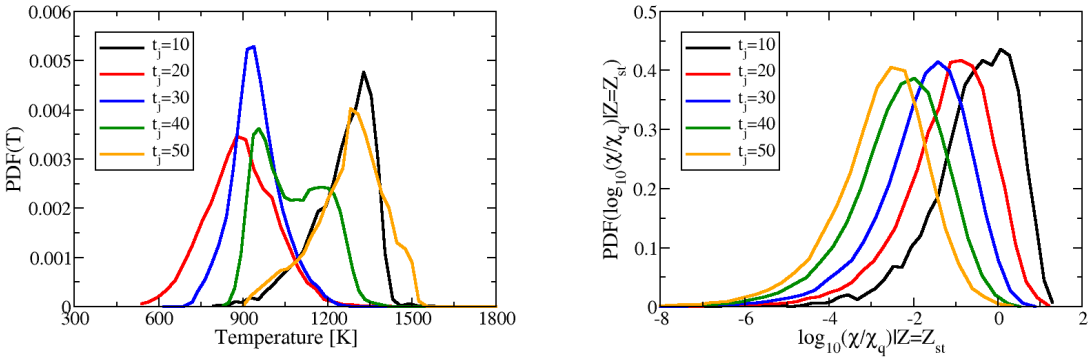

(a) (b)

Figure 18: Evolution of the pdf on stoichiometric plane of (a)temperature and (b)scalar dissipation rate of Z for Case H M-GRID using TANN-2

data for case L and case H F-GRID, respectively, at the location of maximum mean χ_{st} and at $t_j = 40$. The χ distribution reaches much higher values for both the cases at the location of maximum mean χ_{st} compared to the distribution at $t_j = 40$. The maximum χ value observed for case L is around 20,000 where as for case H F-GRID it goes upto 50,000. Thus, χ distribution for case L lies inside the training data space

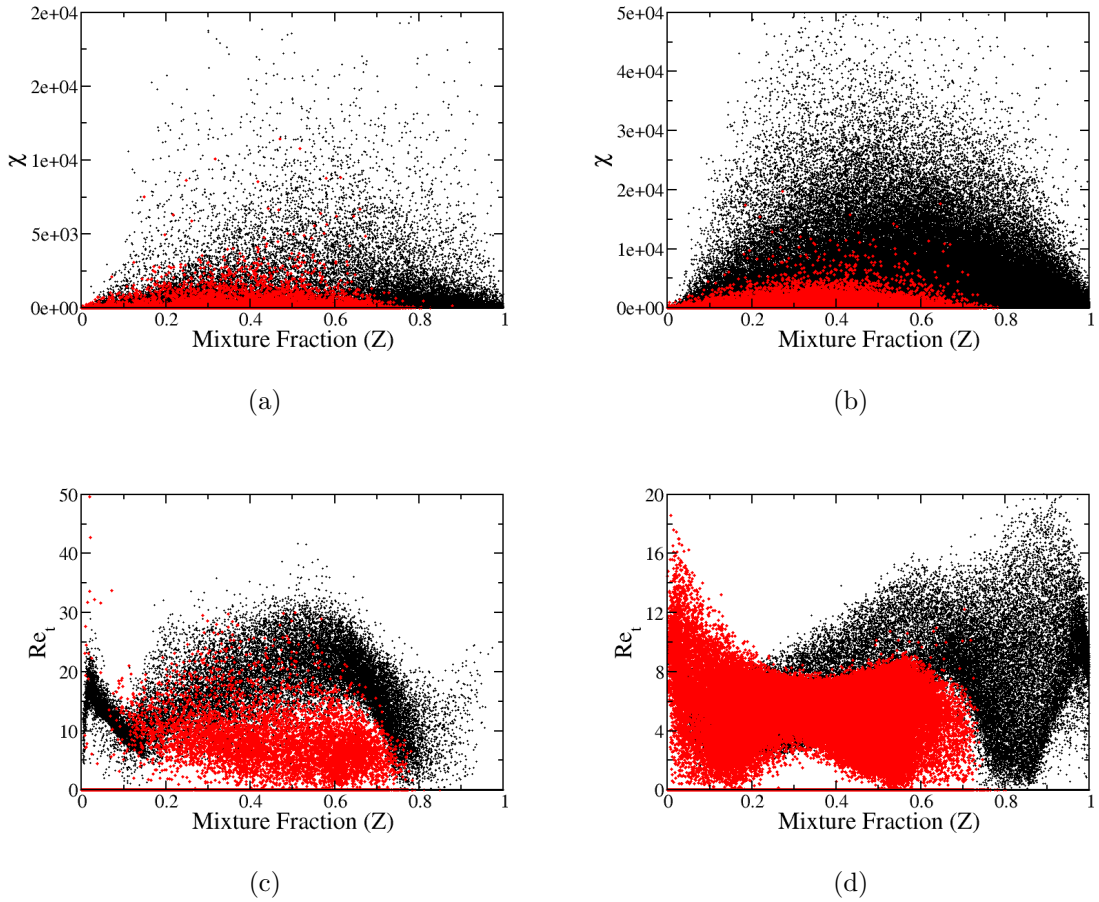

Figure 19: Comparison of χ and Re_t with respect to Z. (a) and (c) represent Case L with Black symbols: $t_j = 15$ and Red symbols: $t_j = 40$. (b) and (d) represent Case H F-GRID with Black symbols: $t_j = 12$ and Red symbols: $t_j = 40$

of both TANN-1 and TANN-2. Whereas, for case H F-GRID χ distribution lies inside the training data space of TANN-2 only. Which is the cause of the failure of TANN-LES using TANN-1 in capturing the extinction-reignition for case H. Fig. 19(c) and 19(d) show the Re_t vs Z data for case L and case H F-GRID, respectively. Both the cases reach the higher Re_t values at the location of maximum χ_{st} compared to $t_j = 40$. The maximum Re_t observed for case L and case H F-GRID are around 40 and 20, respectively. For case H F-GRID the maximum Re_t is lower because of the finer grid size used. Comparing the Re_t distribution of the two cases with Re_t distribution of TANN-1 and TANN-2 training data, it is observed that both TANN-1 and TANN-2

training data cover the Re_t data space of the two test cases.

Fig. 20(a) through 20(d) show the distribution of mass fraction of H_2 and OH vs temperature for case L and case H F-GRID. The thermo-chemical data space for the two cases cover similar regions at extinction or reignition. Based on the comparisons between the training data and the two test cases data, it is observed TANN-1 fails to cover only the χ data space of case H, whereas TANN-2 covers the entire data space of both case L and case H.

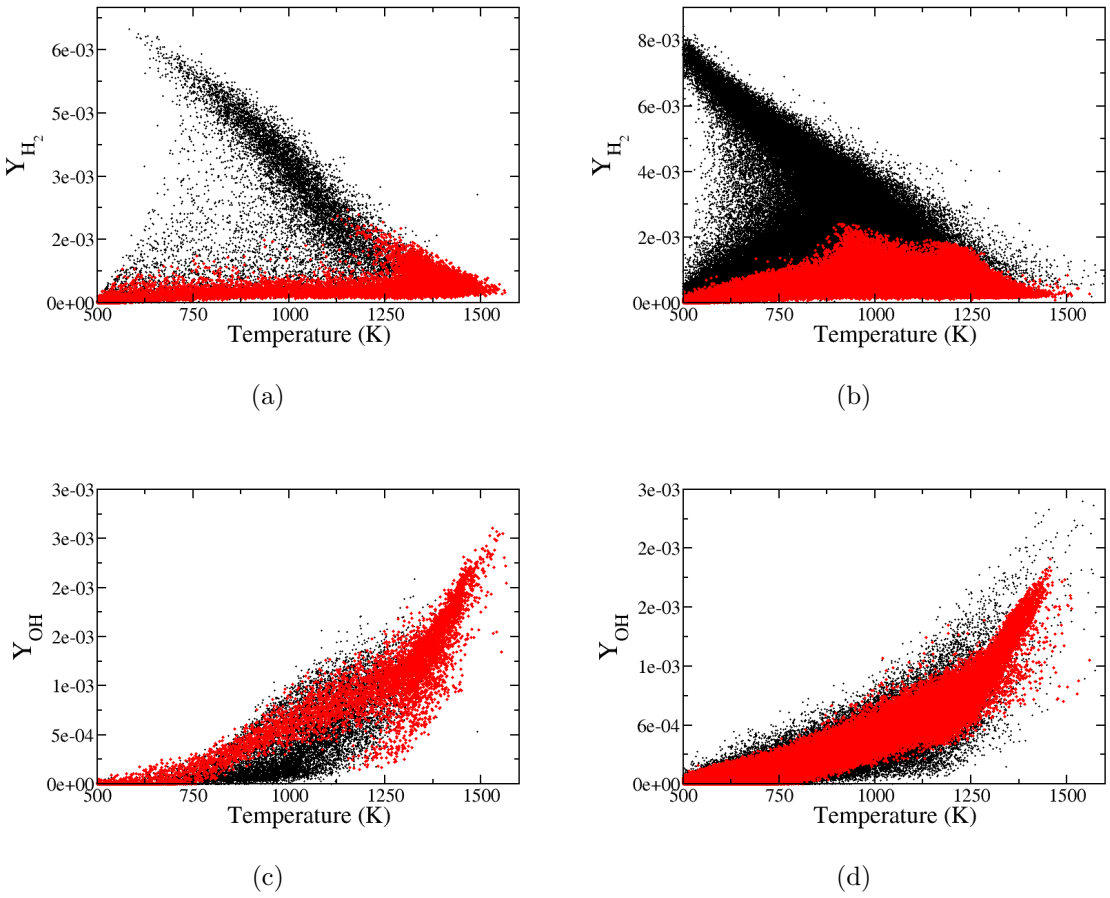

Figure 20: Comparison of H_2 and OH mass fraction with respect to temperature. (a) and (c) represent Case L with Black symbols: $t_j = 15$ and Red symbols: $t_j = 40$. (b) and (d) represent Case H F-GRID with Black symbols: $t_j = 12$ and Red symbols: $t_j = 40$

4.8 Study extinction-reignition using TANN-3 trained as a function of species dissipation rate instead of species gradient

The TANN-LES using TANN-3 net is performed for Case H with M-GRID and the results are compared with DNS and TANN-LES using TANN-2(using species gradient instead of species scalar dissipation rates). As shown in Fig.4.8 no significant difference is observed between the two TANN-LES results.

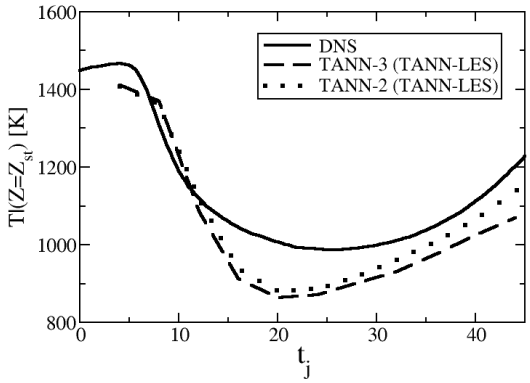

Figure 21: Comparison of mean temperature variation on stoichiometric plane w.r.t. non-dimensional time for Case H M-GRID using TANN-3 and TANN-2

4.9 Time Savings

The computational time required to run a single iteration per grid point on a 220 processors INTEL PC (3.2 GHz Xenon) by DI-LEMLES, LANN-LEMLES and TANN-LES for case H F-GRID are given in table 3. The TANN-LES approach provides a speed-up of 33 times compared to DI-LEMLES with reasonable accuracy, where as LANN-LEMLES provides 6.6 times, for case H.

Table 3: Comparison of speed-up obtained by various models

Case	Model	CPU time per step per cell	speed-up
H F-GRID	DI-LEMLES	4.95 ms	1
	LANN-LEMLES	0.75 ms	6.6
	TANN-LES	0.15 ms	33

CHAPTER V

CONCLUSIONS

In the present work, ANN methodology is used for multi-step finite rate kinetics within the LES framework. Unlike the previous work [34] where ANN was used as a subgrid combustion model within the LES framework (LANN-LEMLES), here ANN is used for calculating the filtered reaction rates directly within the LES framework (TANN-LES). The thermo-chemical data for training the TANN is obtained by filtering the data obtained from a 1D standalone simulation over the LES grid-size [35]. The comparison of the laminar source terms and filtered source terms for the same composition show significant difference. The filtered source terms are trained as a function of the filtered mass fraction of all the species, filtered temperature and the gradient of the species. The species are trained separately.

The TANN-LES is used to simulate the temporally evolving syngas-air diffusion flames, exhibiting significant extinction-reignition, extensively studies by DNS [14] previously. TANN-LES methodology is first validated against DI-LEMLES, LANN-LEMLES and DNS results for the low Re case. The temporal variation of the mean temperature on the stoichiometric plane from TANN-LES results compare well with the DI-LEMLES, LANN-LEMLES with significant speed-up. Comparison with DNS show lower temperature on stoichiometric plane at extinction due to addition of isotropic turbulence in shear layer along a higher thickness, in LES. To further investigate the TANN-LES approach the conditional statistics are extracted and compared with the DNS data at extinction ($t_j = 20$) and reignition ($t_j = 40$). It is observed that the location of the maximum mean temperature does not lie at the stoichiometric mixture fraction due to differential diffusion effects, instead it lies towards the fuel

rich side. The same trend is observed for the H_2O mass fraction. A comparison of the pdf of temperature and H_2O mass fraction indicate slight under prediction of reignition by TANN-LES. Overall, the TANN-LES predictions match well with LEMLES predictions.

The low Re case specific TANN fails to capture the extinction-reignition phenomenon for the high Re case. An attempt is made in generalizing the TANN approach by generating a TANN that can simulate cases with different Re and grid resolutions. The training table for the "generalized" net is generated by running the standalone LEM simulation for a large range of Re_t and an intermediate filter-size. The TANN-LES results using the generalized net obtained for the high Re case with three different grid resolutions compare well with the DNS data, showing grid independence and capability of the generalized net in handling different grid resolutions. Both coarse grid and the fine grid capture the negative-skewness at high scalar dissipation rate in the pdf of the normalized scalar dissipation rate. Comparison of the TANN-LES results for the low Re case using the generalized net with the TANN-LES results using the case specific net show that loss in accuracy by the use of the generalized net is negligible.

A comparison of the training data for the two TANNs with the data from the two Re cases show that both the nets cover the same compositional data space and the thermochemical data from the LES forms a subset of the thermochemical data space of the nets. The χ and the Re_t data space explored by the two nets differ. The Re_t data space of the LES still forms a subset of the training data of the two nets. However, the χ data space of the high Re case falls outside the training data space of the first net which leads to its failure in simulating the high Re case. The χ data space for both Re cases form a subset of the χ data space of the generalized net training data space and hence it is capable of simulating different Re cases. Hence, the current study shows that it is possible to generate a TANN capable of handling

a range of Re. Thus, every new case does not require generation of a new TANN, saving significant time.

To improve the TANN methodology in future, the way of calculating Re_Δ in the 1D standalone LEM code should be explored further. Possibly a k^{sgs}-based u' and LES Δ can be correlated to the LEM u' and the integral length.

APPENDIX A: 21 STEP 11 SPECIES REDUCED SYNGAS MECHANISM

Species:H_2, O_2, OH, H_2O, O, H, HO_2, CO, CO_2, HCO, N_2

$O_2 + H = OH + O$

$H_2 + O = OH + H$

$OH + H_2 = H + H_2O$

$H_2O + O = 2OH$

$H_2 + M = 2H + M$

$2O + M = O_2 + M$

$H + O + M = OH + M$

$OH + H + M = H_2O + M$

$O_2 + H + M = HO_2 + M$

$H + HO_2 = 2OH$

$O + HO_2 = OH + O_2$

$OH + HO_2 = O_2 + H_2O$

$O + CO + M = CO_2 + M$

$O_2 + CO = O + CO_2$

$HO_2 + CO = OH + CO_2$

$OH + CO = H + CO_2$

$HCO + M = CO + H + M$

$O_2 + HCO = HO_2 + CO$

$H + HCO = H_2 + CO$

$O + HCO = H + CO2$

APPENDIX B: TANN COEFFICIENTS

The TANNs generated in the present study have 14 PEs in the input layer. 10, 8 and 4 PEs in the three hidden layers. 1 PE in the output layer, since each species is trained independently. Therefore, the output of ANN training generates ten ANN coefficient tables for the ten reacting species (eleventh species is N_2). Each PE in a given layer transmits signal to all the PEs belonging to layers downstream. The PEs in a given layer do not communicate amongst themselves. This kind of ANN architecture is called an acyclic. Therefore the total number of weight coefficients and biases written in every ANN coefficient table is:

(PEs in input layer) $\times$ $\left(\sum_{n=1}^{n=3}\right.$(PEs in nth hidden layer) + (PEs in output layer))

+ (PEs in 1st hidden layer) $\times$ $\left(\sum_{n=2}^{n=3}\right.$(PEs in nth hidden layer) + (PEs in output layer))

+ (PEs in 2nd hidden layer) $\times$ ((PEs in nth hidden layer) + (PEs in output layer))

+ (PEs in 3rd hidden layer) $\times$ (PEs in output layer)

+ (Sum of PEs in all the layers (bias))

$$\text{Weight connectors} = 14(10+8+3+1)+10(8+3+1)+8(3+1)+3(1) = 496$$

$$\text{Biases} = (14+10+8+3+1) = 37$$

$$\text{Sum of weight connectors and biases} = 496+37 = 533$$

Hence, total number of values tabulated in each TANN coefficient table is 533. Note that bias of PEs in input layer is zero because the PEs in the input layer recieve the full strength of the incoming signal.

Another output of the ANN methodology is the normalizing coefficients of the inputs and de-normalizing coefficients of the outputs. The values of every input in the training table are normalized between -1 to +1, corresponding to minimum and the

maximum input value, respectively. The function used is:

$$\text{Normalized}(\widetilde{Y_{H_2}}) = A_{H_2} \times \widetilde{Y_{H_2}} + B_{H_2}$$

Normalized($\widetilde{Y_{H_2}}$) is the signal transmitted by the PE corresponding to $\widetilde{Y_{H_2}}$ mass fraction in the input layer. Normalizing coefficients A and B are calculated for all the inputs using the same function. The output, source terms in the present study are normalized between -0.8 to +0.8. The source terms are normalized between -0.8 to +0.8, instead of -1 to +1 because the outgoing signal of a PE is obtained by applying hyperbolic tangent function to signal recieved. Therefore, values of -1 and +1 will require the output PE to recieve a signal of strength - and +, respectively. The output of the ANN interpolation for computing source term of H_2 (ANN(H_2)) is de-normalized using the function:

$$\frac{\overline{\omega_{H_2}}}{\overline{\rho}} = \frac{e^{ANN(H_2)} - D_{H_2}}{C_{H_2}}$$

Thus, a table is created in which A and B values corresponding to all inputs, and C and D values corresponding to all outputs are tabulated.

The ANN training gives 10 ANN coefficient files corresponding to each of the 10 reacting species. Each file contains 533 values. An additional table ANN.dat is created which contains the As and Bs corresponding to all inputs, and Cs and Ds corresponding to all outputs.

ANN.dat	format			Sample ANN Cofficient table for a species
A_{H_2}	B_{H_2}	C_{H_2}	D_{H_2}	-3.835612931767081E-002
=	=	=	=	-0.108052176485972
=	=	=	=	-0.436501419823321
A_{N_2}	B_{N_2}	0.0	0.0	0.143977788550831
A_T	B_T	0.0	0.0	5.040344446165773E-003
A_{Re_Δ}	B_{Re_Δ}	0.0	0.0	9.986534201938069E-003
$A_{\bigtriangledown Y_{H_2}}$	$B_{\bigtriangledown Y_{H_2}}$	0.0	0.0	-0.108150477215085
=	=	=	=	=
=	=	=	=	=
$A_{\bigtriangledown Y_{N_2}}$	$B_{\bigtriangledown Y_{N_2}}$	0.0	0.0	=

REFERENCES

[1] Bilger, R., "Some aspects of scalar mixing," *Flow, Turbulence Combust.*, pp. 93–114, 2004.

[2] Blasco, J., Fueyo, N., Dopazo, C., and Ballester, J., "Modelling the temporal evolution of a reduced combustion chemical system with an artificial neural network," *Combust. Flame*, vol. 113, pp. 38–52, 1998.

[3] Boudier, G., Gicquel, L., and Poinsot, T., "Large eddy simulation of soot formation in a turbulent non-premixed jet flame," *Combust. Flame*, vol. 155, pp. 196–214, 2008.

[4] Cha, C., Kosaly, G., and Pitsch, H., "Modelling extinction and reignition in turbulent nonpremixed combustion using a doubly-conditional moment closure approach," *Phys. fluids*, vol. 13, pp. 3824–3834, 2001.

[5] Chakravarthy, V. and Menon, S., "Linear eddy simulations of reynolds and schmidt number dependencies in turbulent scalar mixing," *Physics of Fluids*, vol. 13, pp. 488–499, 2001.

[6] Christo, F., Masri, A., and Nebot, E., "Artificial neural network implementation of chemistry with pdf simulation of h2/co flames," *Combust. Flame*, vol. 106, pp. 406–427, 1996.

[7] Christodoulou, C. and Georgiopoulos, M., *Applications of Neural Networks in Electromagnetics*. Artech House, 2000.

[8] Civco, D., "Artificial neural networks for land-cover classification and mapping," *Int. J. Geographical Information Sci.*, vol. 7, pp. 173–186, 1993.

[9] Cleary, M. and Kronenburg, A., "Multiple mapping conditioning for extinction and reignition in turbulent diffusion flames," *Proc. Combust. Inst.*, vol. 31, pp. 1497–1505, 2007.

[10] DesJardin, P. and Franknel, S., "Large eddy simulation of a nonpremixed reacting jet: Application and assessment of a subgrid-scale combustion models," *Phys. Fluids*, vol. 10, pp. 2298–2314, 1998.

[11] Fureby, C., "Large eddy simulation of turbulent anisochoric flows," *AIAA J.*, vol. 33, pp. 1263–1272, 1995.

[12] Goldin, G. and Menon, S., "A scalar pdf construction model for turbulent non-premixed combustion," *Combust. Sci. and Technol.*, vol. 125, pp. 47–72, 1997.

[13] Goldin, G. and Menon, S., "A comparison of scalar pdf turbulent combustion models," *Combust. Flame*, vol. 113, pp. 442–453, 1998.

[14] Hawkes, E., Sankaran, R., Sutherland, J., and Chen, J., "Scalar mixing in direct numerical simulations of temporally evolving plane jet flames with skeletal co/h2 kinetics," *Proc. Combust. Inst.*, vol. 31, pp. 1633–1640, 2007.

[15] Hilbert, R. and Thevenin, D., "Influence of differential diffusion on maximum flame temperature in turbulent nonpremixed hydrogen/air flames," *Combust. Flame*, vol. 138, pp. 175–187, 2004.

[16] Ihme, M., Marsden, A., and Pitsch, H., "Generation of optimal artificial neural networks using a pattern search algorithm: Application to approximation of chemical kinetics," *Neural Comput.*, vol. 20, pp. 573–601, 2008.

[17] Ihme, M., Schmitt, C., and Pitsch, H., "Optimal artificial neural networks and tabulation methods for chemistry representation in les of a bluff-body swirl-stabilized flame," *Proc. Combust. Inst.*, vol. 32, pp. 1527–1535, 2009.

[18] Kerstein, A., "Linear-eddy model of turbulent scalar transport and mixing," *Combust. Sci. and Tech.*, vol. 60, pp. 391–421, 1988.

[19] Kerstein, A., "Linear eddy model for turbulent transport ii," *Combust. Flame*, vol. 75, pp. 397–413, 1989.

[20] Kim, S., Choi, C., and Huh, K., "Second-order conditional moment closure modeling of a turbulent ch4/h2/n2 diffusion flame," *Proc. Combust. Inst.*, vol. 30, pp. 735–742, 2005.

[21] Kim, W. and Menon, S., "Large eddy simulation of turbulent anisotropic flows," *Int. J. Numer. Methods in Fluids*, vol. 31, pp. 983–1017, 1999.

[22] Kim, W., Menon, S., and Mongia, H., "Large-eddy simulation of gas turbine combustor flow," *Combust. Sci. and Technol.*, vol. 143, pp. 25–62, 1999.

[23] Klimenko, A. and Bilger, R., "Conditional moment closure for turbulent combustion," *Prog. Energy Combust. Sci.*, vol. 25, pp. 595–687, 1999.

[24] Kronenberg, A. and Kostka, M., "Modeling extinction reignition in turbulent flames," *Combust. Flame*, vol. 143, pp. 342–356, 2005.

[25] Mehrotra, K., Mohan, C., and Ranka, S., *Elements of Artificial Neural Networks*. MIT Press, 1997.

[26] Mitarai, S., Kosaly, G., and Riley, J., "A new lagrangian flamelet model for local extinction and reignition," *Combust. Flame*, vol. 137, pp. 306–319, 2004.

[27] Pantano, C., "Direct simulation of non-premixed flame extinction in a methane-air jet with reduced chemistry," *J. Fluid Mech.*, vol. 514, pp. 231–270, 2004.

[28] Peters, N., "Laminar diffusion flamelet model in non-premixed turbulent combustioni," *Prog. Energy Comb. Sci.*, vol. 10, pp. 319–339, 1984.

[29] Peters, N., *Turbulent Combustion*. Cambridge University Press, 2000.

[30] Pitsch, H. and Fedotov, S., "Investigation of scalar dissipation rate fluctuations in non-premixed turbulent combustion using a stochastic approach," *Combust. Theory Modell.*, vol. 5, pp. 41–57, 2001.

[31] Poinsot, T. and Veynante, D., *Theoretical and numerical combustion*. Philadelphia: R T Edwards, 2001.

[32] Sen, B., Hawkes, E., and Menon, S., "Large eddy simulation of extinction and reignition with artificial neural networks based chemical kinetics," *Combust. Flame*, vol. 157, pp. 566–578, 2010.

[33] Sen, B. and Menon, S., "Turbulent premixed flame modeling using artificial neural networks based chemical kinetics," *Proc. Combust. Inst.*, vol. 32, pp. 1606–1611, 2009.

[34] Sen, B. and Menon, S., "Linear eddy mixing based tabulation and artificial neural networks for large eddy simulations of turbulent flames," *Combust. Flame*, vol. 157, pp. 62–74, 2010.

[35] Sen, B. A., *Artificial Neural Networks based Subgrid Chemistry Model for Turbulent Reactive Flow Simulation*. PhD thesis, Georgia Institute of Technology, 2009.

[36] Sripakagorn, P., Kosaly, G., and Pitsch, H., "Local extinction-reignition in turbulent nonpremixed combustion," annual research briefs, Center for turbulence research, 2000.

[37] Sripakagorn, P., Mitarai, S., Kosaly, G., and Pitsch, H., "Extinction and reignition in a diffusion flame: a direct numerical simulation study," *J. Fluid Mech.*, vol. 518, pp. 231–259, 2004.

[38] Veynante, D. and Vervisch, L., "Turbulent combustion modeling," *Progress in Energy and Combustion Science*, vol. 28, pp. 193–266, 2002.

[39] Xu, J. and Pope, S., "Pdf calculations of turbulent nonpremixed flames with local extinction," *Combust. Flame*, vol. 123, pp. 281–307, 2000.

[40] Zhang, G., Patuwo, B., and Hu, M., "Forecasting with artificial neural networks:: The state of the art," *Int. J. Forecasting*, vol. 14, pp. 35–62, 1998.